Sensitive chiral sensing of single-drop solutions by signal-reversing cavity-ringdown polarimetry

a master's thesis authored by

Michail Koutrakis

Supervisor: Prof. Theodore - Peter Rakitzis

MSc. Photonics & Nanoelectronics
Physics Department, University of Crete

June 14, 2022

Acknowledgements

Foremost, I would like to express my sincere gratitude to my supervisor Prof. T. Peter Rakitzis for the support, guidance and motivation during the production of this thesis. I could not have imagined having a better advisor and mentor. Besides my advisor, I would like to thank the rest of my thesis committee: Prof. Iannis Kominis and Dr. Paraskevas Tzallas, for their insightful comments, and questions. I would also like to thank my labmates in Polarization Spectroscopy Group: Dr. Giorgos Katsoprinakis, Michalis Xygkis, Kostas Tazes, Eirini Toutoudaki, Artemis Linaraki and Zoi Sargianni for the discussions, guidance and all the fun we have had in the last year. Special thanks to my friend Filippos Tzimkas-Dakis with whom I had the luck to share an office. Without his encouragement and our endless discussions, the last two years would have been much more difficult. Finally, I would like to thank my family for their unconditional and loving support.

Abstract

Theory and experimental results for chiral cavity-ringdown polarimetry based on ring cavities supporting counter-propagating laser beams are presented. Optical-rotation becomes asymmetric for the two counter-propagating beams in the simultaneous presence of two types of circular birefringence of reciprocal symmetry, namely chiral optical activity and Faraday rotation. This asymmetry allows the implementation of signal-reversing measurement techniques, which enable rapid background subtractions, which, in turn, result in reduced common mode noise levels and, ultimately, to higher Signal-to-Noise Ratios and better sensitivities. We present measurements of the specific rotation of tartaric acid and lysozyme at 532 nm. We also present measurements of human and artificial tears. All measurements were performed using a 40 μl cell, a volume approximately two orders of magnitude smaller than cell volumes used in commercial instruments. The current apparatus surpasses commercial polarimeters by providing tangible improvements in every aspect: sensitivity, time resolution, and sample volume.

Contents

Chapter 1

Introduction

The purpose of the present thesis is the precise estimation of chiral angles in volumes approximately one hundred times smaller than those of commercial instruments, using a bowtie cavity and implementing signal reversals. At first, we present the most important properties of chirality (Chapter 2). Specifically, we examine its definition and the role it plays in physical sciences. Next, we describe the relationship between optical activity and chirality as well as a simple way to measure it using two linear polarizers. Finally, we study the magneto-optic, Faraday effect, which, as chirality, is responsible for the rotation of the plane of polarization of linearly polarized light. In Chapter 3 we present two cavity ring-down techniques, cavity ring-down spectroscopy (CRDS), and cavity ring-down polarimetry (CRDP), which are prerequisites in understanding the experiment conducted here, CRDP with signal reversals. The experimental technique implemented is thoroughly presented in Chapter 4. We start by describing the advantages of our approach as well as we derive the most important relations we used in our analysis. Furthermore, we give a detailed description of the experimental setup followed by the presentation of our measurements. Finally, we discuss our results and make suggestions for future improvements. It is worth mentioning that the technique described here was first developed by our group approximately ten years ago [1] opening the field in measurements of optical activity using four-mirror cavities.

This page intentionally left blank.

Chapter 2

Chirality

2.1 Definition

Chirality is a physical property of matter related to its symmetry characteristics. The term "chiral" is derived from the Greek *kheir*, meaning "hand", which is the most famous chiral object. In 1904, Lord Kelvin stated about chirality, *" I call any geometrical figure, or group of points, chiral, and say it has chirality, if its image in a plane mirror, ideally realized, cannot be brought to coincide with itself "* [2].

However, the concept of chirality does not apply only to stationary objects, but also to time-dependent physical entities represented by vectors and vector fields, either static or changing, some of them originating in translational or rotational movement [3]. In 1986, L D Barron proposed an extended definition of chirality by introducing the terms "true chirality" and "false chirality". According to Barron, a system exhibits true chirality if there exists a second system, known as an enantiomer, which

1. is obtained by space inversion of the former and they are not superimposable, and
2. the two systems are not interconverted by time reversal.

The absence of the second requirement leads to the condition known as "false chirality" [3, 4].

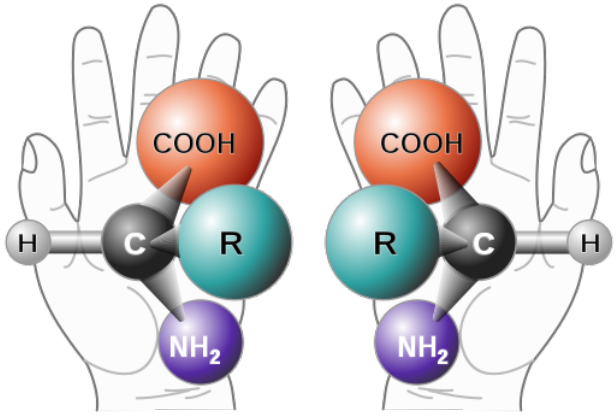

Figure 2.1: Chirality demonstrated by human hands and two enantiomers of a generic amino-acid. Image source: `https://en.wikipedia.org/wiki/File:Chirality_with_hands.svg`

2.2 Historical Background & Importance

Chirality first came into the spotlight in the early 19th century, when scientists tried to explain the peculiar properties of symmetric objects like crystals. Quartz determined a vital role. Mineral quartz was the first material in which optical rotation[1] was observed, in 1811 by the French mathematician F.Arago [5]. Later, in 1812, J.B. Biot discovered that natural quartz existed in two forms that rotated in opposite directions the plane of polarization of light emerging through them. Furthermore, he discovered a linear relationship between the angle of rotation and the thickness of the quartz as well as he introduced the polarimeter as a scientific tool [3].

It was not until Fresnel's contribution to the theory of transverse waves, that the scientific community understood that linearly polarized light is a superposition of left and right circularly polarized light. They concluded that optical rotation was the consequence of the different refractive indices between left and right circularly polarized light inside a chiral substance.

In the middle 19th century, J.B. Biot and Louis Paster studied two substances with the same molecular formulas (i.e., isomers) and came up with extraordinary results. The two isomeric substances studied, were the optically active (+)-tartaric acid and the optically inactive paratartaric acid with formulas $C_4H_6O_6$ (Figure 2.2). The two substances differ in crystal morphology as it had been discovered by the mineralogist E. Mitscherlich. Paster prepared crystals of the substances mentioned above and showed that although both of them were hemihedral (i.e., a property of symmetry), in the (+)-tartare the hemihedral facets were all facing in the same direction, whereas in the paratartare there were equal amounts of crystals with hemihedral facets having either this orientation or the opposite, forming a crystal that eventually is optically inactive [3]. Although it seemed reasonable that highly organized structures like crystalline solids (e.g., quartz or tartrate salts) are optically active, the fact that optical activity, was observed in aqueous solutions of tartares (i.e., not organized structures) led to the conclusion that *chirality is a property of the molecules themselves.*

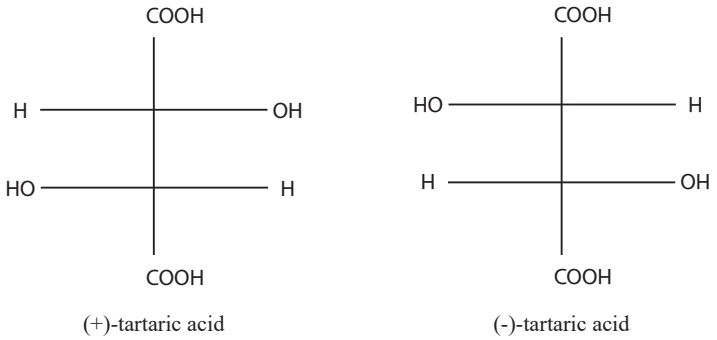

Figure 2.2: Tartaric acid enantiomers. Optically inactive substance contains equal amount of (+) and (-)-tartaric acid.

[1]Optical rotation is the rotation of the plane of linearly polarized light exhibited when the light beam passes through an optically active medium. More on optical activity in Section 2.3.

The two equivalent types of chiral molecules are called enantiomers. Each enantiomer is the mirror image of the other. With further study on chiral molecules, it was observed that nature displays a preference for one of the two enantiomers in most organic molecules. For the time being, numerous theories have been developed to explain this mystery but a definite interpretation has yet to be given. However, it has been experimentally verified [6–9] that chirality is strongly connected with the fundamental force of nature known as the "weak interaction" or "weak force".

Although the origin of chirality has not been clarified yet, chirality is a fundamental property of existence. Living organisms rely on chiral molecules since almost all biological molecules such as proteins, nucleic acids, and sugars are chiral. A fascinating aspect of chiral molecules is that both enantiomers of a chiral molecule share the same qualities (e.g., vapor pressure, density, etc.) but react differently with other chiral molecules. For example, one enantiomeric form of a chiral molecule inside a drug might be a medicine for a particular disease whereas the opposite enantiomer, may not only be inactive but can also be toxic.

Chiral sensing and chiral analysis are essential in several scientific subfields of chemistry, biology, physics, and medicine, and in the food, pharmaceutical, and cosmetic industries. Among its many usages, chirality detection can aid drug design and synthesis, contribute to protein structure determination and help detect parity violation of the weak force [10].

The similar characteristics of the two enantiomers of a chiral substance, urge us to detect chirality by examining the interaction between the chiral molecules and light. Specifically, in order to determine the type of chirality, we examine the light polarization and how it is affected by a property of chiral substances called "optical activity".

2.3 Optical Activity

Optically active substances change the state of polarization of a beam of polarized light. Specifically, materials composed of chiral molecules tend to rotate the plane of polarization of linearly polarized light that passes through them. The physical mechanism behind the optical activity is based on the fact that right and left circularly polarized light is differently absorbed in chiral molecules, a phenomenon known as circular dichroism.

Here, we derive an equation for the angle ϕ by which the linearly polarized light will be rotated. We assume that light propagates along the z-axis and the electric and magnetic field of right and left circularly polarized light are described by:

$$\mathbf{E}_\eta = \frac{E_0}{\sqrt{2}} (\hat{\mathbf{x}} - i\eta\hat{\mathbf{y}}) \tag{2.1a}$$

$$\mathbf{B}_\eta = \frac{E_0}{\sqrt{2}} (i\eta\hat{\mathbf{x}} + \hat{\mathbf{y}}) \tag{2.1b}$$

where $\eta = +$ and $\eta = -$ describe left and right circularly polarized light respectively.

We define the ground and the excited molecule states as $|g\rangle$ and $|e\rangle$ respectively. The

electric dipole (E1) and magnetic dipole (M1) transition amplitudes are:

$$E1 = \langle e|\mathbf{E1}|g\rangle \tag{2.2a}$$

$$M1 = \langle e|\mathbf{M1}|g\rangle \tag{2.2b}$$

where

$$\mathbf{E1} = \sum_i e\mathbf{r}_i \tag{2.3a}$$

$$\mathbf{M1} = -\frac{e\hbar}{2m_e c}\left(\mathbf{L} + 2\mathbf{S}\right) \tag{2.3b}$$

is the electric dipole moment operator and the magnetic dipole moment operator respectively.

It is well known from quantum theory that the **E1** operator allows transitions between states of opposite parity (even $\leftrightarrow$ odd) whereas the **M1** operator allows transitions between states of the same parity (even $\leftrightarrow$ even or odd $\leftrightarrow$ odd). As a result, in a nonchiral molecule, where every state is either even or odd, transitions can be either E1 or M1, but not both. We note that for pure E1 or M1 transitions there is no circular dichroism, namely:

$$|E1|^2 = |\langle e|\mathbf{E1}\cdot\mathbf{E}_+|g\rangle|^2 = |\langle e|\mathbf{E1}\cdot\mathbf{E}_-|g\rangle|^2 \tag{2.4a}$$

$$|M1|^2 = |\langle e|\mathbf{M1}\cdot\mathbf{B}_+|g\rangle|^2 = |\langle e|\mathbf{M1}\cdot\mathbf{B}_-|g\rangle|^2 \tag{2.4b}$$

Contrary to nonchiral molecules that have well-defined parity states, the molecular states of chiral molecules have both even and odd characters, so that a superposition of E1 and M1 transitions can occur [11]. The transition amplitude A_η is given by:

$$A_\eta = \langle e|\mathbf{E1}\cdot\mathbf{E}_\eta + \mathbf{M1}\cdot\mathbf{B}_\eta|g\rangle \tag{2.5}$$

We define the asymmetry factor δ as:

$$\delta = \frac{|A_+|^2 - |A_-|^2}{|A_+|^2 + |A_-|^2} = \frac{2\,\mathrm{Im}\left(E1\cdot M1\right)}{|E1|^2 + |M1|^2} \approx 2\,\mathrm{Im}\left(\frac{M1}{E1}\right) \tag{2.6}$$

The asymmetry factor is a quantity capable of identifying the concentration of a specific chiral molecule. Generally, it ranges from 10^{-6} to 10^{-3} since M1 transitions are a lot weaker than E1.

The relation we obtain for circular dichroism by using the dispersion relations [12] is:

$$\delta = \frac{|A_+|^2 - |A_-|^2}{|A_+|^2 + |A_-|^2} = \frac{n_L - n_R}{2\left(n-1\right)} \tag{2.7}$$

where n_L and n_R are the refractive indices for left and right circularly polarized light respectively and $n = \left(n_L + n_R\right)/2$. For chiral molecules, it applies that $n_L \neq n_R$ (circular birefringence) leading to the rotation of linearly polarized light by an angle ϕ.

Chiral angle ϕ can be derived by expressing linearly polarized light as a superposition of left and right circularly polarized light. We assume linearly polarized light along the x-axis with electric field $\mathbf{E}$.

Using Jones notation (appx. A) we have:

$$\underbrace{\begin{bmatrix}1\\0\end{bmatrix}}_{\tilde{E}_{0x}} = \frac{1}{\sqrt{2}}\left(\underbrace{\frac{1}{\sqrt{2}}\begin{bmatrix}1\\i\end{bmatrix}}_{\tilde{E}_{0L}} + \underbrace{\frac{1}{\sqrt{2}}\begin{bmatrix}1\\-i\end{bmatrix}}_{\tilde{E}_{0R}}\right) \tag{2.8}$$

where $\tilde{E}_{0x}$, $\tilde{E}_{0L}$, $\tilde{E}_{0R}$ are the Jones vectors for linearly, left and right circularly polarized light respectively.

For an optically inactive medium the velocities v_L and v_R inside the medium, of left and right circularly polarized light respectively, are equal. Since $v = c/n$ and $k = n\omega/c$ the relationship $v_L = v_R$ is equivalent with $n_L = n_R$ and $k_L = k_R$. Figure 2.3 illustrates the vector addition of left and right circularly polarized light that produces linearly polarized light along the x -axis at three different times in an oscillation. The vector sum $\mathbf{E}$ oscillates along the x-axis as the $\mathbf{E_R}$ and $\mathbf{E_L}$ vectors rotate at equal rates clockwise and counterclockwise, respectively.

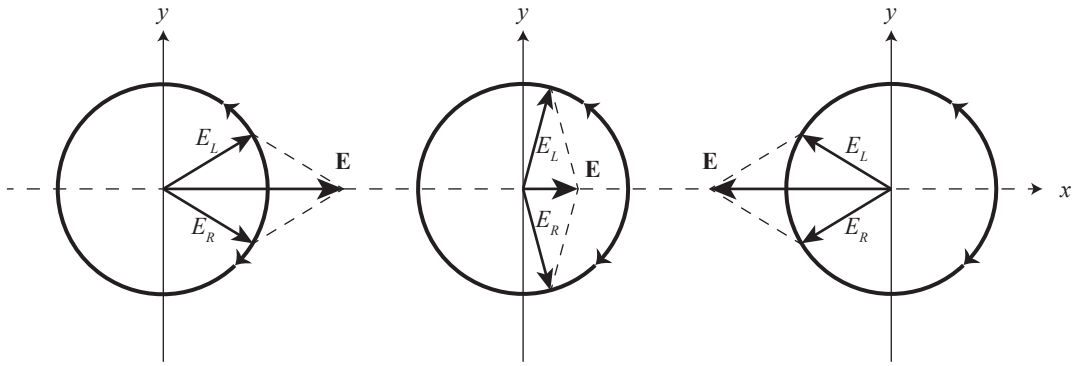

Figure 2.3: Vector sum of the electric field $\mathbf{E} = \mathbf{E_R} + \mathbf{E_L}$ inside an optically inactive medium at different instances. $\mathbf{E_R}$ and $\mathbf{E_L}$ vectors rotate clockwise and counterclockwise, respectively, at equal rates. Light emerges from the page.

For an optically active medium $n_L \neq n_R$ or $k_L \neq k_R$. The fact that the two wavevectors are not equal for the two components, $\mathbf{E}_L$ and $\mathbf{E}_R$, leads to different phase terms, θ_L and θ_R respectively. In general, the complex electric fields of the two components can be expressed as:

$$\mathbf{E}_L = \tilde{\mathbf{E}}_{0L} e^{i(k_L d - \omega t)} = \tilde{\mathbf{E}}_{0L} e^{i\theta_L} \tag{2.9a}$$

$$\mathbf{E}_R = \tilde{\mathbf{E}}_{0R} e^{i(k_R d - \omega t)} = \tilde{\mathbf{E}}_{0R} e^{i\theta_R} \tag{2.9b}$$

where d is the light path inside the chiral medium, $\theta_L = (k_L d - \omega t)$ and $\theta_R = (k_R d - \omega t)$.

Suppose that for an active medium we have $k_L > k_R$. After the light travels a distance d into the medium, we have $\theta_L > \theta_R$ for all t. This situation is depicted at an arbitrary

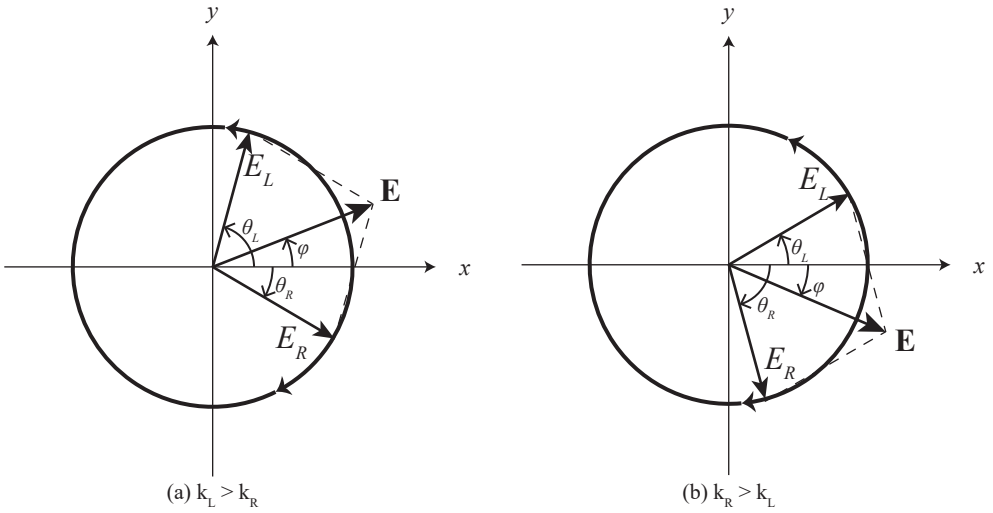

Figure 2.4: Optical rotation inside a chiral medium. The left and right circularly polarized light travel at different speeds. (a) $k_L > k_R$ and (b) $k_R > k_L$. The light is assumed to be emerging from the page.

instant in Figure 2.4(a). The vector sum of $\mathbf{E}_L$ and $\mathbf{E}_R$ is once more linearly polarized light but with an inclination angle $+\phi$ relative to the x-axis (i.e., the initial polarization axis). In Figure 2.4(b) the opposite case is depicted, where angle ϕ is negative.

The magnitude of ϕ can be obtained by noticing that $\mathbf{E}$, is always the diagonal of an equal-sided parallelogram and as a result, it bisects opposite angles, so that:

$$\theta_L - \phi = \theta_R + \phi$$

or

$$\phi = \frac{1}{2}\left(\theta_L - \theta_R\right) \tag{2.10}$$

Substituting θ_L and θ_R in (2.10) we obtain:

$$\phi = \frac{1}{2}\left(k_L - k_R\right) d \tag{2.11}$$

Finally, using $k_L = 2\pi n_L/\lambda$ and $k_R = 2\pi n_R/\lambda$, we obtain:

$$\boxed{\phi = \frac{\pi d}{\lambda}\left(n_L - n_R\right)} \tag{2.12}$$

where λ is the light wavelength and d is the pathlength inside the chiral substance. Using (2.6) and (2.7) ϕ can be written as:

$$\phi = \frac{2\pi d}{\lambda}\left(n - 1\right)\delta = \frac{4\pi d}{\lambda}\,\mathrm{Im}\left(\frac{M1}{E1}\right) \tag{2.13}$$

Equation (2.13) elucidates that, since $\mathrm{Im}\,(M1/E1)$ is a property of the molecule, the chiral angle ϕ can be maximized by maximizing n and d as well as choosing λ to be small. The refractive index n is capable of being increased by means of increasing the sample concentration and by choosing a wavelength near an optical resonance [11]. Although the

above requirements are theoretically applicable, their experimental complexity turns us to find a way to increase the effective pathlength d. For that reason, optical cavities are extensively used in the study of chirality, as they allow the light beam to travel a large distance inside the chiral sample.

In general, the net angle of rotation ϕ due to a light path d through an optically active substance of density ρ is given by:

$$\boxed{\phi = \alpha \cdot d \cdot \rho} \tag{2.14}$$

where α is the specific rotation of the substance with units [deg $\mathrm{dm}^{-1}\mathrm{g}^{-1}\mathrm{mL}$]. Specific rotation is a characteristic value of the substance and it is wavelength dependent.

2.4 Single-pass Measurement of Optical Activity

Optical activity is easily measured using two linear polarizers (appx. A.2), LP1 and LP2 as depicted in Figure 2.5. At first, the transmission axes (TA) of the two polarizers are placed with perpendicular orientations. As a consequence, the light will pass through LP1 but not through LP2, Figure 2.5(a). When we place an optically active material between the two polarizers the condition of light extinction no longer exists. The $\vec{\mathbf{E}}$-vector of the light is rotated by ϕ due to the optically active medium and as a result, the TA of LP2 is no longer perpendicular to the new plane of polarization, Figure 2.5(b). The angle of rotation ϕ can be precisely measured by rotating the second polarizer until extinction reoccurs. Single-pass measurements are applicable only when the physical properties of the optically active material create relatively large chiral angles ($> 1°$).

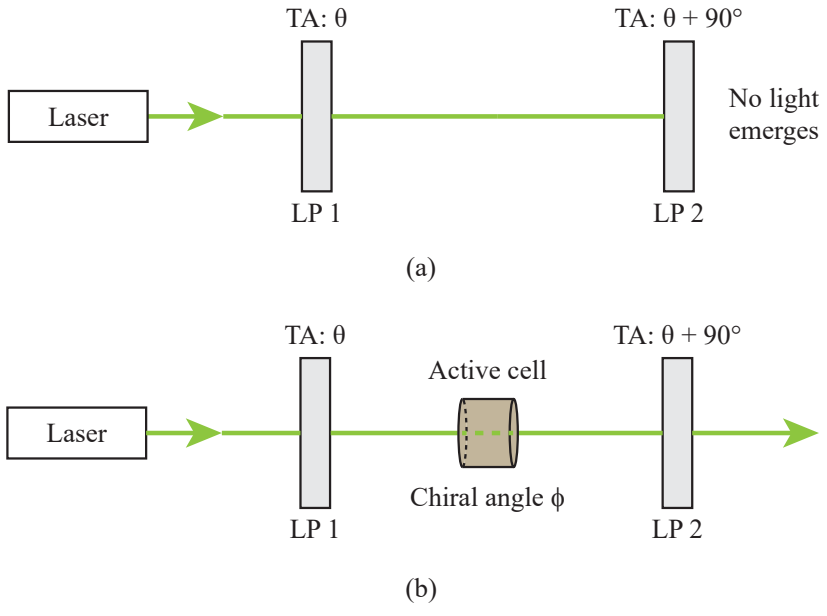

Figure 2.5: Single-pass measurement of optical activity. (a) The two polarizers (LP1 and LP2) have crossed transmission axes (TA) and as a result, no light emerges through LP2. (b) When a chiral medium is inserted between LP1 and LP2, the state of polarization of light reaching LP2 is no longer perpendicular to its TA. As a result, light passes through.

2.5 Faraday Effect

Apart from optical activity, another physical mechanism that is responsible for the rotation of linearly polarized light is the Faraday effect. Faraday effect is one of the most important magneto-optic effects. When certain materials (Faraday rotators) are placed inside a longitudinal magnetic field, parallel to the propagation of light, they become capable of rotating the polarization of linearly polarized light that passes through them (Figure 2.6). Specifically, linearly polarized light passing through a magneto-optic material exhibits a net rotation θ_F of the plane of polarization proportional both to the thickness d of the material and the strength of the magnetic field B:

$$\theta_F = VBd \tag{2.15}$$

where V is the Verdet constant of the material. The Verdet constant is both temperature and wavelength dependent with units $[\text{rad}/(T \cdot m)]$.

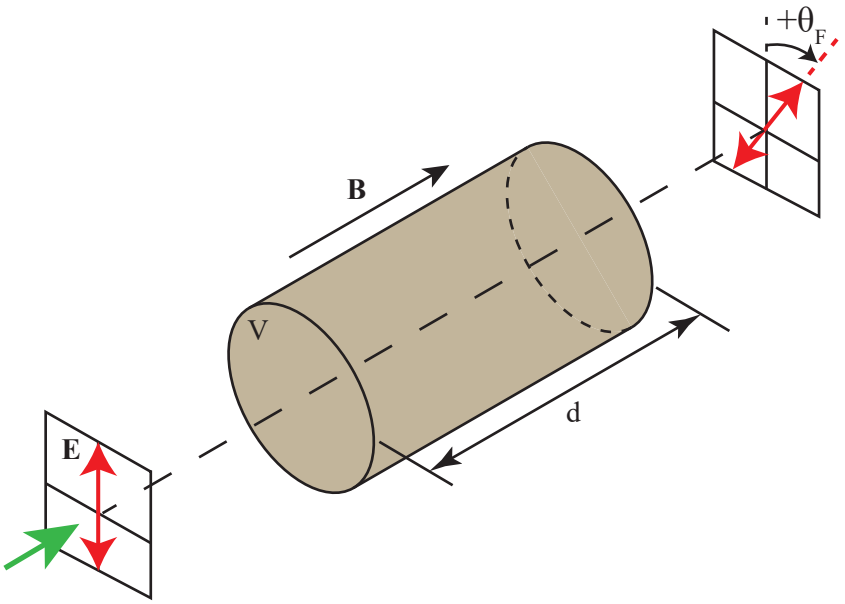

Figure 2.6: Faraday effect. A magneto-optic material, with Verdet constant V, is placed parallel to a uniform, static magnetic field **B** causing rotation of the plane of polarization of initially vertically polarized light by an angle θ_F.

An essential property of the Faraday effect is that the sense of rotation relative to the magnetic field direction is *independent* of the propagation direction of the light and depends only on the direction of the magnetic field (Figure 2.7(a),(b)). That is not the case for chiral rotation, where the sense of rotation depends on the direction of propagation of the beam (Figure 2.7(c),(d)). Thus, repeated forward and backward traversals of a Faraday rotator by a light beam have a cumulative effect on the angle of rotation. On the other hand, when a light beam passes forward and backward successively through a chiral substance, the net chiral angle will be zero $(\phi + (-\phi) = 0)$.

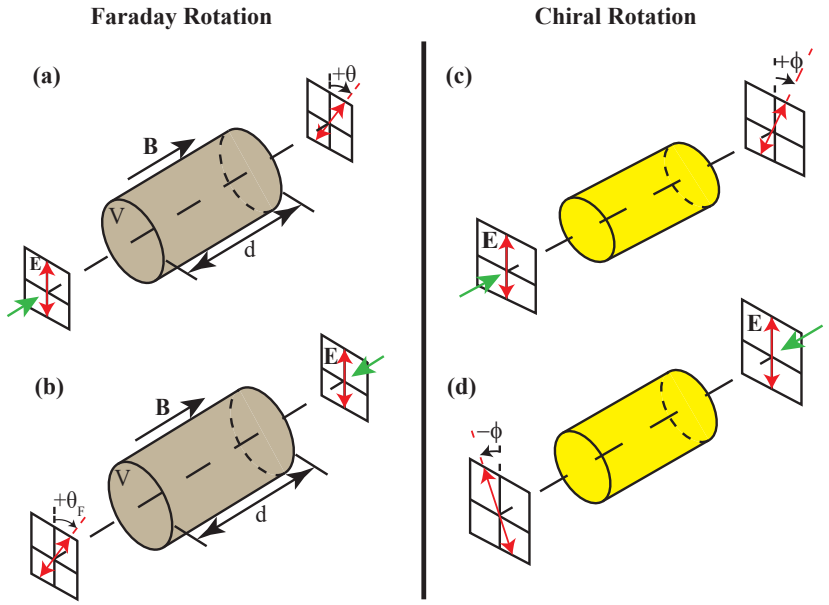

Figure 2.7: Faraday rotation vs chiral rotation (lab frame). (a), (b) show that the sense of rotation is independent of the propagation direction of the light and depends only on the direction of the magnetic field. (c), (d) show that optical activity depends on the direction of propagation of the beam.

Depending on the wavelength of interest, there are plenty of magneto-optic crystals that can be used as Faraday rotators. The most widely used crystal below $1100nm$ is terbium-gallium-garnet $Tb_3Ga_5O_{12}$, known as TGG. However, recently, a crystal with Verdet constant similar to TGG has been developed. Cerium fluoride, CeF_3, crystal seems to absorb less than TGG in a wider spectral region [13]. Cerium fluoride had a vital role in the present thesis as it will be apparent in Chapter 4. In Figure 2.8 the dependence of CeF_3 Verdet constant is given as a function of wavelength in room temperature [13].

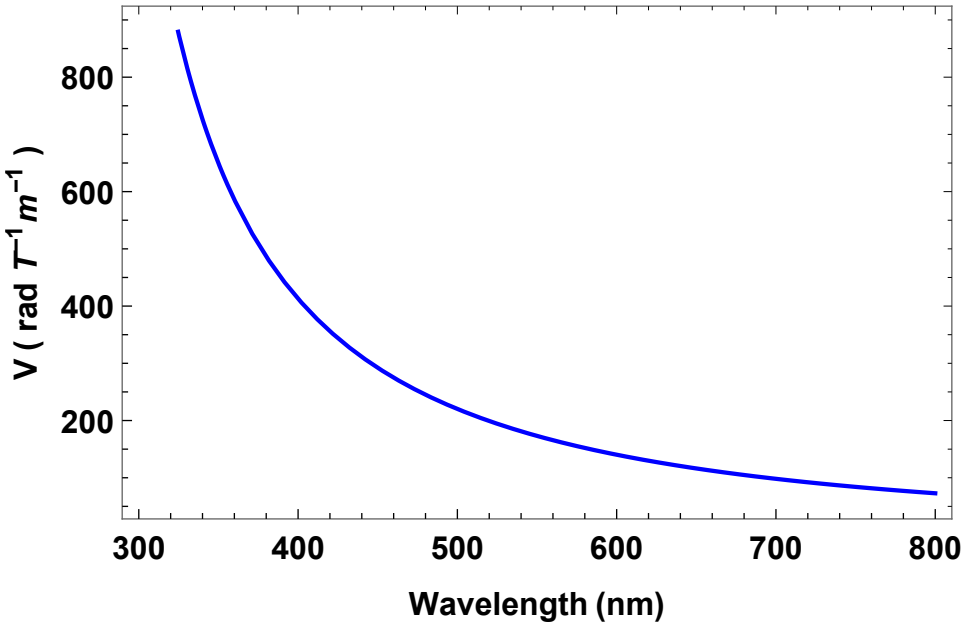

Figure 2.8: Verdet constant dependence on wavelength for Faraday rotator CeF_3. $V = E/(\lambda^2 - \lambda_0^2)$ where $E = 42474.1 \times 10^3$ rad nm^2/(T m), $\lambda_0 = 239$ nm and λ is the wavelength [13].

The principal application based on the Faraday effect is the optical isolator. The general configuration of an optical isolator is shown in Figure 2.9. The configuration consists of a polarizer-analyzer pair and a Faraday rotator between them. The magnetic field and the characteristics of the crystal must fulfill the requirement to have a Faraday angle of $\theta_F = 45°$. Assuming that the initial polarizer is at an angle θ with the x-axis then the second polarizer (analyzer) must be at an angle $\theta + \theta_F = \theta + 45°$. This configuration allows the light passing through the first polarizer to emerge through the analyzer. The essential feature of this setup is, that due to the symmetry characteristic of Faraday rotation, light back-reflected from the optical system (retro-pulses) is rotated an additional 45° in *the same rotational sense* so that it emerges perpendicular to the axis of the first polarizer. As a result, light cannot return to where it came. This application is of great importance since retro-pulses can create critical damage to laser systems.

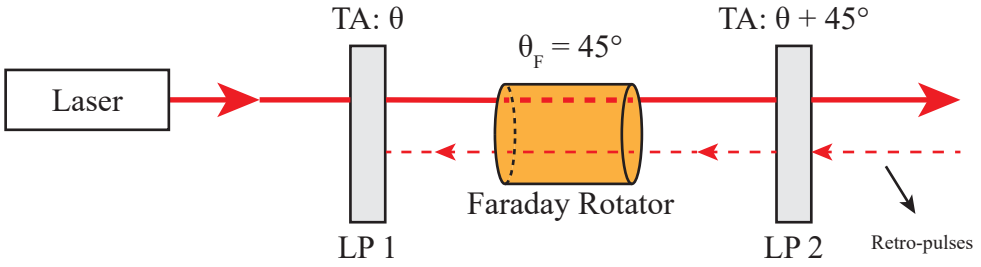

Figure 2.9: Optical isolator configuration. Because of the Faraday rotator, light returning from the rest of the optical system (retro-pulses) is lineraly polarized, perpendicular to the transmission axis (TA) of the first polarizer (LP1). As a result it does not return to the laser.

Chapter 3

Cavity Ring-Down Techniques

Optical resonators or optical cavities are configurations that aim at trapping light between mirrors. The general idea behind optical cavities is that the geometrical characteristics of the cavity (e.g. distance between mirrors, their radius of curvature, etc.) create certain conditions that light must fulfill to survive between the mirrors. For a cavity to be stable, i.e. the ray position stays "close" to the optical axis even after many transits between the mirrors, the geometry must be chosen so that the size of the beam does not continually grow with multiple reflections. For that purpose, it is a common practice to place lenses before the cavity entrance in order to modify the spatial characteristics of the beam (appx. C.3).

For continuous wave (cw) lasers, light confined in the cavity reflects on the mirrors, travels inside the cavity multiple times and as a result, it interferes with itself producing standing waves with different standing frequencies. Specifically, in order for a standing wave to be formed, the cavity length must be an integral number of the wavelength. The standing wave patterns produced are called modes. The definition of a cavity mode given by Verdeyen [14] is the following: "A cavity mode is a field distribution that reproduces itself in relative shape and in relative phase after a round trip through the system".

Although optical cavities are usually related to cw experiments, they also find implementation with pulsed lasers. For pulsed lasers, the situation is slightly different. When the duration of the pulses emitted by the laser is short (Section 3.1), the light traveling inside the cavity does not interact with itself in a single roundtrip. As a result, standing waves are not formed and the pulse goes back and forth between the mirrors, as long as the cavity is stable and the spatial characteristics of the beam are correct. Configurations with pulsed lasers offer robustness, since they allow easy cavity alignment because they are less affected by changes in the cavity length. Hence, they are extensively used for various kinds of measurements, such as absorption (Section 3.1), ellipsometry [15–19] , and polarimetry (Section 3.2).

3.1 Cavity Ring-Down Spectroscopy (CRDS)

Very sensitive detection techniques for measuring absorption have been developed with optical cavities. Optical cavities, filled with the absorbing species, enormously increase the absorption length by allowing light to pass repeatedly through the sample.

Cavity Ring-Down Spectroscopy (CRDS) is based on measurements of the decay times of optical cavities filled with the absorbing substance. This technique is generally implemented using short laser pulses, with a pulse duration less than the time the light needs to travel a complete roundtrip, $\tau_{pulse} < t_{rt}$. The pulse will be reflected back and forth between the mirrors, while for each roundtrip a small fraction will be transmitted through the end mirror and reach the detector, as depicted in Figure 3.1 [20]. The absorption is detected by measurement in the decrease in the photon lifetime τ in the cavity (compared to an empty cavity, with $\tau = \tau_0$), which appears as an exponential decay, or "ring-down".

In the following sections, we derive the ring-down time for empty (τ_0) and filled (τ) cavities using both the "traditional" approach as well as matrix treatment of polarization described in appendix A.

3.1.1 Empty Cavity

First, we examine an empty cavity of length d consisting of two mirrors (Figure 3.1). We assume that the two mirrors have different reflection and transmission coefficients $R_1 = r_1^2$, $T_1 = t_1^2$, and $R_2 = r_2^2$, $T_2 = t_2^2$ respectively, where without loss of generality, we consider the amplitude coefficients r_1, t_1, r_2, t_2 to be real.

We also assume that light entering the cavity is linearly polarized with electric field $\mathbf{E_0} = E_0\hat{\mathbf{x}}$. In the current approach, we will ignore the vector nature of the electric field.

The electric field of a single laser pulse after it passes through the two mirrors, *without* traveling a complete roundtrip, is:

$$E_0' = t_2 \cdot t_1 \cdot E_0 \tag{3.1}$$

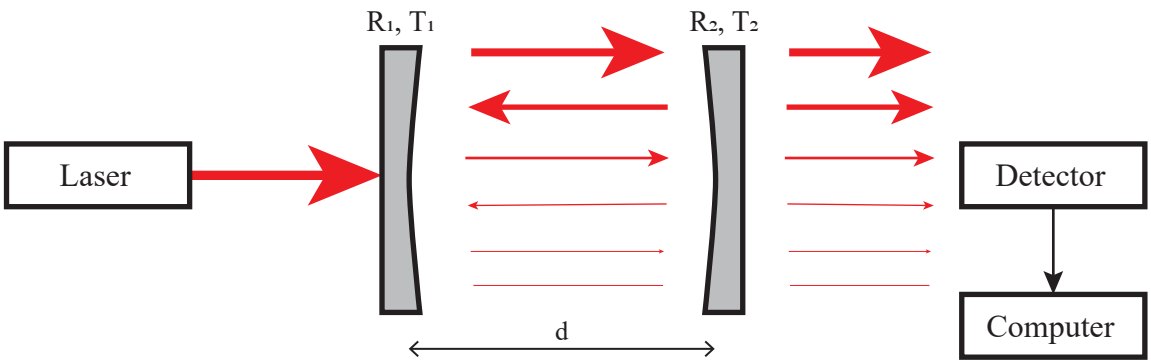

Figure 3.1: CRDS configuration consisting of two mirrors, with reflection and transmission coefficients R_1,T_1 and R_2,T_2 respectively, separated by a distance d. Pulse duration is less than the roundtrip time, $\tau_{pulse} < t_{rt}$.

The electric field after a single roundtrip is:

$$\begin{aligned} E_1 &= t_2 \cdot r_1 \cdot r_2 \cdot t_1 \cdot E_0 \\ &= (r_1 \cdot r_2) \cdot E_0' \end{aligned} \tag{3.2}$$

After the second roundtrip:

$$\begin{aligned} E_2 &= t_2 \cdot r_1 \cdot r_2 \cdot r_1 \cdot r_2 \cdot t_1 \cdot E_0 \\ &= (r_1 \cdot r_2)^2 \cdot E_0' \end{aligned} \tag{3.3}$$

By induction, we conclude that after N roundtrips:

$$\begin{aligned} E_N &= (r_1 \cdot r_2)^N \cdot E_0' \\ &= \left((r_1 \cdot r_2)^2\right)^{N/2} E_0' \\ &= (R_1 R_2)^{N/2} E_0' \end{aligned} \tag{3.4}$$

For the light intensity we have:

$$I_N = |E_N|^2 \tag{3.5a}$$
$$= I_0 \cdot (R_1 R_2)^N \tag{3.5b}$$
$$= I_0 \cdot e^{N \ln(R_1 R_2)} \tag{3.5c}$$
$$\approx I_0 \cdot e^{N(R_1 R_2 - 1)} \tag{3.5d}$$

where $I_0 = |E_0'|^2$. From (3.5c) to (3.5d) we approximated $\ln(x)$ as $\ln(x) \approx x - 1$ for x around 1, as is the case for the reflection coefficients $R_1 R_2$.

If we replace N with $N = \frac{t}{t_{rt}}$,where $t_{rt} = \frac{2d}{c}$ is the roundtrip time, equation (3.5) can be written as:

$$\boxed{I(t) = I_0 \cdot e^{-\frac{t}{\tau_0}}} \tag{3.6}$$

where τ_0 is the ring-down time given by:

$$\tau_0 = \frac{t_{rt}}{1 - R_1 R_2} \tag{3.7}$$

In the special case where the two mirrors have the same reflection amplitudes $r_1 = r_2 = r$ equation (3.4) is written as:

$$E_N = R^N \cdot E_0' \tag{3.8}$$

Similarly for the light intensity we have:

$$I_N = I_0 \cdot e^{2N(R-1)} \tag{3.9}$$

As a result:

$$I(t) = I_0 \cdot e^{-\frac{t}{\tau_0}} \tag{3.10}$$

where

$$\tau_0 = \frac{t_{rt}}{2(1-R)} = \frac{d/c}{1-R} \tag{3.11}$$

As an example we can consider a cavity with $R_1 = R_2 = R = 0.999$ and $L = 30cm$. We find $t_{rt} = 2ns$. Equation (3.7) gives $1.0005\mu s$ and equation (3.11) gives exactly $1\mu s$.

For a four-mirror bow-tie empty cavity of length L, with mirror reflectivities R_1, R_2, R_3, R_4 (Figure 3.2), equation (3.6) still applies with τ_0 given by:

$$\tau_0 = \frac{t_{rt}}{1 - R_1 R_2 R_3 R_4} \tag{3.12}$$

with roundtrip time $t_{rt} = \frac{L}{c}$.

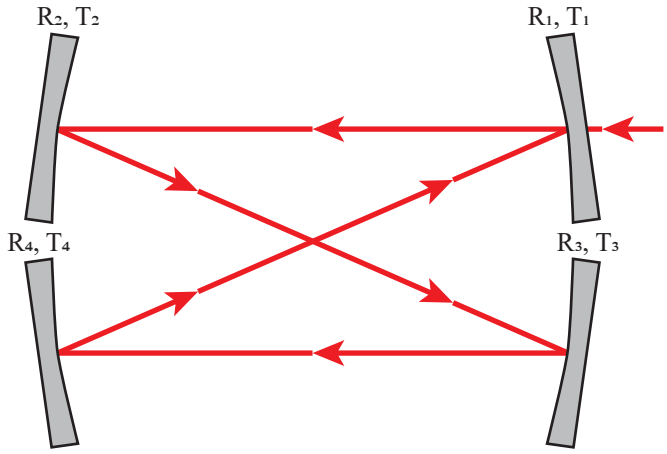

Figure 3.2: Four-mirror, bowtie, empty cavity.

Next, we derive the ring-down time for an empty cavity using "Jones calculus" (appx A). As explained in appx. A.2 the final polarization state of light emerging from any kind of configuration, P_f, can be derived by multiplying the matrix representing the whole configuration, J_f, with the initial polarization vector, P_i.

$$P_f = J_f P_i \tag{3.13}$$

From table A.3 the Jones matrix representation of a mirror with a finite reflectivity R ($0 \leq R \leq 1$) is given by:

$$J_{M_i}(R_i, \delta_i) = \sqrt{R_i} \begin{bmatrix} -e^{i\delta_i/2} & 0 \\ 0 & e^{-i\delta_i/2} \end{bmatrix} \tag{3.14}$$

Assuming normal incidence, the phase shifts δ_i are taken to be approximately zero.

We assume that the initial polarization vector, P_i , is given by:

$$P_i = \frac{1}{\sqrt{|\alpha_i|^2 + |\beta_i|^2}} \begin{bmatrix} \alpha_i \\ \beta_i \end{bmatrix}, \quad \alpha_i, \beta_i \in \mathbb{C} \tag{3.15}$$

which represents the most general polarization state, elliptical polarization.

For a two-mirror cavity with mirror reflectivities R_1 and R_2, J_f^1, after one roundtrip, is given by:

$$J_f^1 = J_{M_1}(R_1, 0) J_{M_2}(R_2, 0) \tag{3.16}$$

and after N roundtrips:

$$J_f^N = (J_{M_1} J_{M_2})^N = \begin{bmatrix} \left(\sqrt{R_1 R_2}\right)^N & 0 \\ 0 & \left(\sqrt{R_1 R_2}\right)^N \end{bmatrix} \tag{3.17}$$

From (3.17) we obtain:

$$P_f = J_f^N P_i = \frac{1}{\sqrt{|\alpha_i|^2 + |\beta_i|^2}} \begin{bmatrix} \left(\sqrt{R_1 R_2}\right)^N \alpha_i \\ \left(\sqrt{R_1 R_2}\right)^N \beta_i \end{bmatrix} \equiv \begin{bmatrix} \alpha_f \\ \beta_f \end{bmatrix} \tag{3.18}$$

As a result:

$$I_f \propto |P_f|^2 = |\alpha_f|^2 + |\beta_f|^2 = (R_1 R_2)^N \tag{3.19}$$

Following the same procedure as the one described in (3.5) we obtain:

$$I(t) \propto e^{-\frac{t}{\tau_0}} \tag{3.20}$$

where the ring-down time τ_0 is given by:

$$\tau_0 = \frac{t_{rt}}{1 - R_1 R_2} \tag{3.21}$$

From equations (3.6), (3.7), (3.20) and (3.21) we conclude that the two methods reproduce the same results, as expected.

In Figure 3.3 we present the intensity of light for $N = 80$ consecutive passes inside the cavity. The light intensity depicted drops exponentially as it was expected.

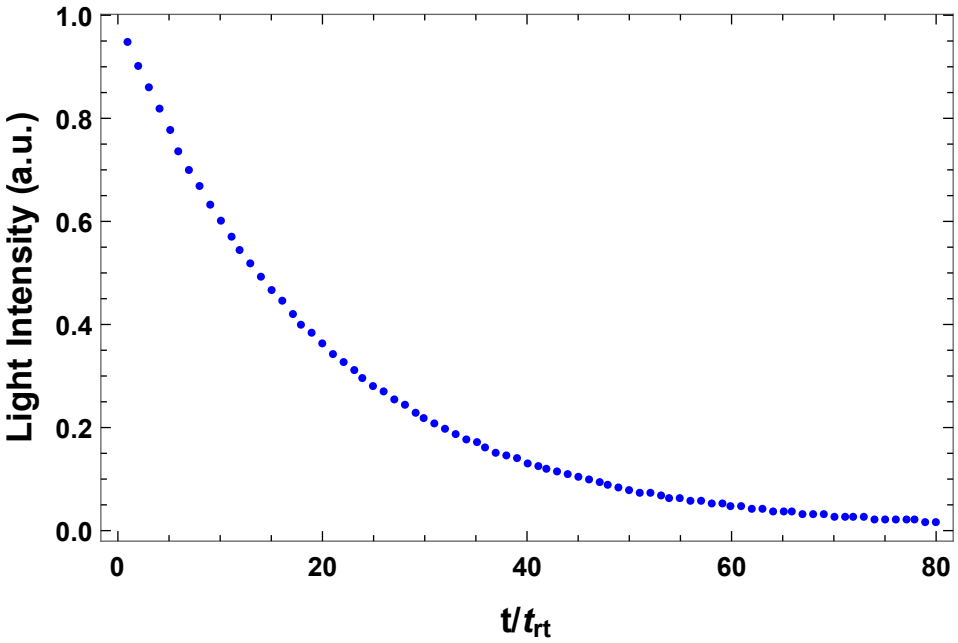

Figure 3.3: Simulation of light intensity as a function of time in a CRDS experiment. We considered mirror reflectivities $R_1 = 0.97$ and $R_2 = 0.98$ and $P_i = \begin{bmatrix}1\\0\end{bmatrix}$. Light intensity drops exponentially as expected.

Similarly, for a four-mirror cavity (Figure 3.2):

$$J_f^N = (J_{M_1} J_{M_4} J_{M_3} J_{M_2})^N = \begin{bmatrix} \left(\sqrt{R_1 R_2 R_3 R_4}\right)^N & 0 \\ 0 & \left(\sqrt{R_1 R_2 R_3 R_4}\right)^N \end{bmatrix} \tag{3.22}$$

As a result (3.20) is still applicable with:

$$\tau_0 = \frac{t_{rt}}{1 - R_1 R_2 R_3 R_4} \tag{3.23}$$

identical to (3.12).

We conclude that the form of the ring-down time τ_0 does not depend on the number of cavity mirrors since it can always be written as:

$$\boxed{\tau_0 = \frac{t_{rt}}{1 - R_{tot}}} \tag{3.24}$$

where R_{tot} is the total reflectivity of the cavity.

3.1.2 Filled Cavity

Next, we examine the case of a two-mirror cavity whose interior is not empty but instead, it contains an optical component (e.g. a laser window) that consists of two surfaces (Figure 3.4). We assume that each surface has transmission coefficient $X = x^2$, where x is assumed real.

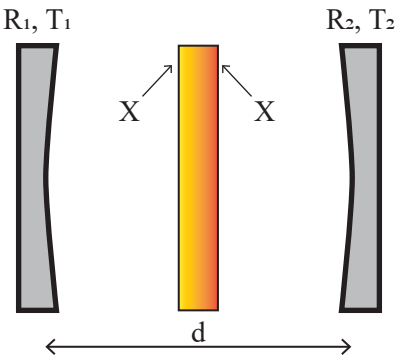

Figure 3.4: CRDS configuration of a two-mirror cavity filled with an optical component. Each surface of the optical component has transmission coefficient X.

Following the same procedure as the one described in 3.1.1, we obtain:

$$E_0' = t_2 \cdot x \cdot x \cdot t_1 \cdot E_0 \tag{3.25}$$

After a single roundtrip we have:

$$\begin{aligned} E_1 &= t_2 \cdot x \cdot x \cdot r_1 \cdot x \cdot x \cdot r_2 \cdot x \cdot x \cdot t_1 \cdot E_0 \\ &= (r_1 \cdot r_2) \cdot x^4 \cdot E_0' \end{aligned} \tag{3.26}$$

We conclude that after N roundtrips:

$$\begin{aligned} E_N &= (r_1 \cdot r_2 \cdot x^4)^N \cdot E_0' \\ &= \left(\left(r_1 \cdot r_2 \cdot x^4\right)^2\right)^{N/2} \cdot E_0' \\ &= \left(R_1 R_2 X^4\right)^{N/2} \cdot E_0' \end{aligned} \tag{3.27}$$

As a result:

$$\begin{aligned} I_N &= |E_N|^2 \\ &= I_0' \cdot \left(R_1 R_2 X^4\right)^N \\ &= I_0' \cdot \ e^{N \ln(R_1 R_2 X^4)} \\ &\approx I_0' \cdot \ e^{N(R_1 R_2 X^4 - 1)} \end{aligned} \tag{3.28}$$

where $I_0 = |E_0'|$ and $\ln(R_1 R_2 X^4) \approx R_1 R_2 X^4 - 1$ since $R_1 R_2 X^4 \approx 1$.

Replacing N with $N = \frac{t}{t_{rt}}$ we obtain:

$$I(t) = I_0 \cdot e^{-\frac{t}{\tau}} \tag{3.29}$$

where τ is the ring-down time:

$$\tau = \frac{t_{rt}}{1 - R_1 R_2 X^4} \tag{3.30}$$

The same result can be obtained by "Jones calculus". We describe each surface of the absorbing element with the following 2×2 matrix:

$$J_{abs} = \begin{bmatrix} x & 0 \\ 0 & x \end{bmatrix} \tag{3.31}$$

where we assumed that the absorption is the same for both polarization components. As a result:

$$J_f^N = (J_{M_1} J_{abs} J_{abs} J_{M_2} J_{abs} J_{abs})^N = \begin{bmatrix} X^2\sqrt{R_1 R_2} & 0 \\ 0 & X^2\sqrt{R_1 R_2} \end{bmatrix} \tag{3.32}$$

Following the same procedure as the one described in section 3.1.1 we obtain identical results with (3.29) and (3.30).

Equation (3.30) can be generalized as:

$$\boxed{\tau = \frac{t_{rt}}{1 - R_{tot} A}} \tag{3.33}$$

where A corresponds to the total absorption coefficient of the substance inside the cavity. Equation (3.33) holds for cavities with two or more mirrors.

The coefficient A can be obtained using the relations (3.24) and (3.33). Solving for R_{tot} in (3.24) we obtain:

$$R_{tot} = 1 - \frac{t_{rt}}{\tau_0} \tag{3.34}$$

Using (3.34) and (3.33) we obtain:

$$\boxed{A = \frac{\tau_0}{\tau}\left(\frac{\tau - t_{rt}}{\tau_0 - t_{rt}}\right)} \tag{3.35}$$

For the case examined above $A = X^4$.

The result (3.35) puts the spotlight on the importance of cavity ring-down spectroscopy. By simply measuring the ring-down times for empty and filled cavity the absorption of a substance inside the cavity can be precisely estimated.

3.2 Cavity Ring-Down Polarimetry (CRDP)

Cavity Ring-Down Polarimetry (CRDP) can be considered as an extension of CRDS since it is based on both optical cavities and pulsed lasers but instead of absorption measurements, it is used for the determination of circular dichroism and circular birefringence of different substances.

CRDP was first implemented in a two-mirror cavity [21,22]. In principle, the measurement of chiral rotation cannot be performed in a simple cavity consisting of two mirrors, as the chiral optical rotation of the light beam through the sample is exactly canceled by the chiral rotation of the returning beam. Two possible solutions to this problem are the following:

1. In contrast to a two-mirror cavity, a ring cavity, consisting of three or more mirrors, allows the light to travel a complete roundtrip by passing through the sample from the *same direction* only once. This solution is the main idea behind the present thesis and it will be thoroughly explained in Chapter 4.

2. Instead of placing the sample inside a simple two-mirror cavity, we insert two, low-loss, quarter wave plates (appx. A.2) in the cavity on either side of the sample with their optical axis at an angle $(90^\circ - \alpha)$ to each other, where α is a small angle, $\alpha \approx 3^\circ$ [21–23].

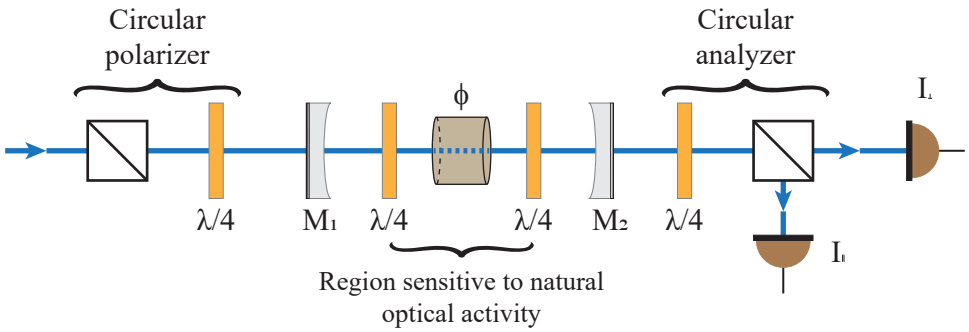

Figure 3.5: Experimental configuration for two-mirror CRDP. Two, low-loss, quarter wave plates are placed in the cavity on either side of the sample with their optical axis at an angle $(90^\circ - \alpha)$ to each other, where $\alpha \approx 3^\circ$ [21].

Here, we examine the second solution which was first implemented by Vaccaro et.a [21]. In Figure 3.5 the experimental configuration used in [21] is depicted. The light inserting the cavity is circularly polarized. Due to the two quarter-wave plates, the light between them is linearly polarized. For an empty cavity the linearly polarized light is rotated by an angle 2α per cavity round trip, as we will show below using "Jones Calculus".

We assume that the light entering the cavity is right circularly polarized described by the following Jones vector:

$$P_i = \frac{1}{\sqrt{2}} \begin{bmatrix} 1 \\ -i \end{bmatrix} \tag{3.36}$$

For simplicity, we assume that the fast-axis (FA) of each quarter-wave plate has a finite angle with the x-axis. The first quarter-wave plate has its FA parallel with the x-axis while the second quarter-wave plate at an angle $(90^\circ - \alpha)$.

After the light passes the first quarter-wave plate it turns into linearly polarized with an angle 45° with the x-axis:

$$J_{\lambda/4}(0^\circ)P_i = \frac{1}{\sqrt{2}} \begin{bmatrix} e^{-\frac{i\pi}{4}} & 0 \\ 0 & e^{\frac{i\pi}{4}} \end{bmatrix} \begin{bmatrix} 1 \\ -i \end{bmatrix} = \frac{1-i}{2} \begin{bmatrix} 1 \\ 1 \end{bmatrix} = \frac{1-i}{\sqrt{2}} \begin{bmatrix} \cos(\frac{\pi}{4}) \\ \sin(\frac{\pi}{4}) \end{bmatrix} \tag{3.37}$$

After the light passes through the two quarter-wave plates it reflects on the mirror and passes again through the second quarter-wave plate but having the opposite direction. As

a result, we change the angle $(90^\circ - \alpha) \rightarrow -(90^\circ - \alpha)$ for the second waveplate.

$$J_{\lambda/4}(-(90^\circ - \alpha))\ J_{M_2}(R,0)\ J_{\lambda/4}(90^\circ - \alpha)\ J_{\lambda/4}(0^\circ)P_i = -\left(\frac{1+i}{\sqrt{2}}\right)\sqrt{R}\begin{bmatrix}\cos(\frac{\pi}{4}+2\alpha)\\ \sin(\frac{\pi}{4}+2\alpha)\end{bmatrix} \tag{3.38}$$

where we used the matrix defined in (3.14) to describe the cavity mirror with reflectivity R.

From equation (3.38) we conclude that the plane of linearly polarized light has been rotated by 2α.

When a chiral substance is inserted in the cavity, the chiral rotation is ϕ_c per cavity pass and $2\phi_c$ per cavity round trip, which gives a total rotation of $2(\alpha + \phi_c)$ per cavity roundtrip.

So far, apart from the two quarter-wave plates nothing seems to differ from the CRDS setup. The situation changes when we place a polarizer at the cavity output before the detector. In this case equation (3.6), $I(t) = I_0 e^{-t/\tau}$ is modified. In addition to the exponential decay, there is also an oscillating term, from the polarization rotation. As a result the signal recorded by the detectors will be of the form[1]:

$$\boxed{I(t) = I_0\ e^{-\frac{t}{\tau}} \cos^2(\omega t + \xi)} \tag{3.39}$$

where ω is the polarization rotation frequency, given by

$$\omega = \frac{\text{total angle of rotation in a single roundtrip}}{\text{roundtrip time}} \tag{3.40}$$

and ξ is just a phase term.

For an empty cavity we have:

$$\omega_0 = \frac{2\alpha}{t_{rt}} = \frac{\alpha c}{d} \tag{3.41}$$

where t_{rt} is the cavity roundtrip time, $t_{rt} = 2d/c$ where d is half the total optical path length. When the cavity is filled with a chiral substance:

$$\omega_c = \frac{2\,(\alpha + \phi_c)}{t_{rt}} = \frac{(\alpha + \phi_c)\,c}{d} \tag{3.42}$$

Using equations (3.41) and (3.42) we obtain:

$$\phi_c = \frac{(\omega_c - \omega_0)\,d}{c} \tag{3.43}$$

From equation (3.43) we conclude that by knowing the polarization beating frequencies for empty and filled cavity, we can accurately estimate the single-pass chiral optical rotation angle.

[1] Equation (3.39) is one of the most important equations of the present thesis. It is analytically derived in Chapter 4.

At this point, we will examine the importance of a significantly large polarization rotation inside the cavity. First, the fact that the angle 2α is large leads to a signal with numerous oscillations in a time interval approximately equal to the ring-down time τ. As a result, the beating frequencies ω_0 and ω_c can be easily estimated. The second advantage is that the rotation of polarization in every roundtirp leads to suppression of undesired linear birefringence within the cavity, maintaining the linear polarization with insignificant depolarization. In Figure 3.6 we present the mechanism for birefringence suppression which is thoroughly explained in [11].

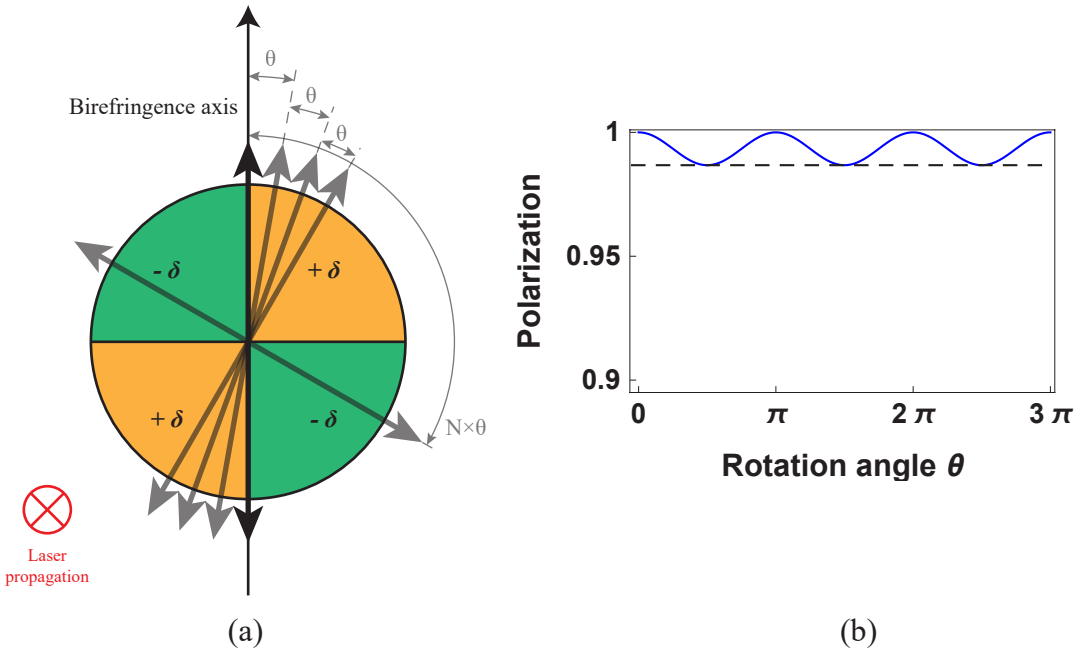

Figure 3.6: (a) Protection of linear polarization by intracavity circular birefringence as the linear polarization rotates through positive and negative linear birefringence. (b) The degree of polarization of the light oscillates, with small amplitude, about a value close to 1. [11]

We assume that the light propagates in a direction perpendicular to the figure plane. The linear polarization rotates by 2α per cavity roundtrip and therefore completes a half rotation after $90°/\alpha$ cavity roundtrips. For an angle of $\alpha \approx 3°$ we have $90°/\alpha \approx 30$ which is much less than the total number of cavity roundtrips inside a typical cavity. From Figure 3.6 we notice that the birefringence for the second quarter turn has the opposite sign to that of the first quarter turn. Therefore, for the first quarter turn, the birefringence acquired by the light beam is exactly cancelled by that acquired in the second quarter turn. Hence, the degree of linear polarization decreases during the first quarter turn and reaches a minimum, but then increases and reaches the original degree of linear polarization by the end of the second quarter turn. This cycle is repeated for each half turn, and on average the degree of linear polarization remains high ($> 90\%$) as long as the intracavity circular birefringence angle is much larger than the cavity linear birefringence angle [11].

Using CRDP, Vaccaaro and coworkers have measured the specific rotation of several molecules in gas phase and extrapolated the results for solution phase. The results are presented in Table 3.1.

Through CRDP, a quantitive method for measuring chiral optical rotation with a cavity was developed. The essential point of this method is that the chiral signals are proportional to the number of cavity passes N and therefore can be enhanced by about $N \approx 1000$ for a high finesse cavity. In addition, the ability to suppress linear birefringent backgrounds using large intracavity circular birefringence consists of an important breakthrough as linear birefringence is one of the most common factors limiting polarimetry measurements [11].

Chiral Sample	Purity	Wavelength (nm)	Specific Rotation (deg $dm^{-1}g^{-1}mL$) Gas Phase (Measured)	Specific Rotation (deg $dm^{-1}g^{-1}mL$) Solution Phase (Extrapolated)
(+)-α-Pinene	>99% (97%ee)	355	+191.2 ± 2.8	+165.2
(+)-α-Pinene	>99% (97%ee)	633	+48.1 ± 1.9	+45.5
(-)-α-Pinene	>99% (97%ee)	355	-188.8 ± 2.8	-165.2
(-)-β-Pinene	>99% (97%ee)	355	+70.5 ± 2.0	+21.8
(-)-β-Pinene	>99% (97%ee)	633	-12.1 ± 1.9	-17.0
(-)-*cis*-Pinane	>99%	355	-63.0 ± 5.9	-88.4
(+)-*cis*-Pinane	>99%	633	+5.2 ± 1.1	+19.0
(+)-Limonene	>99% (97%ee)	355	+304.2 ± 11.0	+416.9
(-)-Fenchone	>98%	355	-180.3 ± 9.3	-157.8
(-)-Propylene oxide	>99%	355	+10.2 ± 2.9	+26.4

Table 3.1: Gas- and Solution-Phase Specific Rotation Measurements of Chiral Samples, from [21, 22].

Chapter 4

CRDP with Signal Reversals

In this chapter, we give a detailed description of the experiment conducted (i.e., CRDP with signal reversals) to measure the optical activity of single-drop chiral solutions. Measurements of solutions of lysozyme and tartaric acid as well as human and artificial tears are presented, followed by a discussion on the results and suggested improvements for the future.

4.1 Basic Principles

In the previous chapter we described how Vaccaro and coworkers developed a method of chiral measurement using a two-mirror optical cavity. Although that approach increased significantly the effective length of the sample leading to increased sensitivity, there still were some issues needed to be solved. The limiting factor, for both single-pass (Section 2.4) and two-mirror cavity-enhanced cases is the ability to measure the null sample. The null sample can be the empty cavity in the case of gas-phase measurements or the solvent inside of which a chiral solution has been mixed. The measurement of the null sample often introduces instability to the overall measurement system. The act of removing the sample might cause small changes to the alignment, the positioning, background birefringence or contamination of the measurement cell/chamber of the chiral sample. In this chapter, we describe a method that allows the absolute measurement of the chiral signals, without needing to remove the sample.

In contrast to the linear cavity shown in Figure 3.5, we now consider a *ring cavity* shown in Figure 4.1. The main difference between a ring and a linear cavity is the fact that a ring cavity can support two separate directions of propagation. The two directions are usually labeled as CW, clockwise, and CCW, counterclockwise. Furthermore, the output from these two directions can be easily spatially separated, in contrast to a linear cavity where spatial separation is more difficult.

As it was explained in Section 3.2 the crucial component of a CRDP configuration is the large intracavity circular birefringence. Apart from protecting the linear polarization from linear birefringence, it also creates signals with numerous oscillations leading to a better estimation of the polarization beating frequency. In Vaccaro's work that kind of

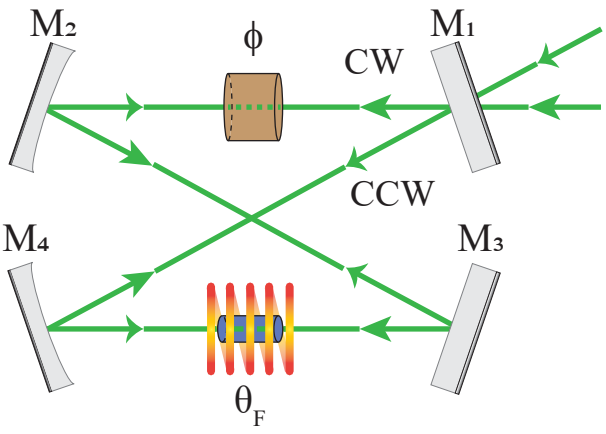

Figure 4.1: Four-mirror, bowtie cavity for CRDP experiment. The light for both propagation directions, CW and CCW, enters into the cavity through mirror M_1. The chiral sample produces an chiral angle ϕ, while the faraday angle θ_F is produced by a CeF_3 crystal inside a uniform magnetic field generated by a coil. In the laboratory frame of reference, the sign of chiral angle differs for each propagation direction whereas the sign of θ_F depends only on the direction of the magnetic field.

circular birefringence was produced by two quarter-wave plates with optical axes offset by an angle $90 - \alpha$ producing a chiral rotation of angle 2α per roundtrip. The angle is *chiral* because the sign of the angle is determined by the propagation direction, in the laboratory frame. Therefore, if a chiral sample placed inside the cavity produces an rotation angle ϕ_c, the total single-roundtrip rotation angle will be $(2\alpha + \phi_c)$ for both CW and CCW directions.

However, this is not the case for rotation produced using the Faraday Effect, described in Section 2.5. Using transparent magneto-optic crystals with a large Verdet constant, such as TGG or CeF_3, allows the creation of circular birefringence of the same order of magnitude as in Vaccaro's work. By examining Figure 2.8 in Section 2.5, we conclude that a CeF_3 crystal with length 5 mm, inside a magnetic field of ≈ 800 G, at 532 nm can produce faraday angle of approximately 8°, which is of similar magnitude to that produced using the quarter-wave plates. Such magnetic fields can be produced with solenoids and can be reversed in sign from $+B$ to $-B$, at will. Therefore, we see that intracavity circular birefringence can be produced magneto-optically.

In the laboratory frame of reference, the sign of Faraday rotation angle θ_F is determined only by the direction of the magnetic field. This difference in symmetry, compared to the chiral rotation, leads to a remarkable result when both directions of propagation are present in a ring cavity. When intracavity circular birefringence is produced using the Farday effect instead of the two quarter-wave plates, the symmetry between CW and CCW breaks, leading to different total single-pass rotation angles Θ_{cw} and Θ_{ccw}, as in one case the two angles add and in the other case the two angles subtract:

$$\Theta_{cw} = \theta_F + \phi_c \tag{4.1a}$$

$$\Theta_{ccw} = \theta_F - \phi_c \tag{4.1b}$$

In analogy to equation (3.40), the different single-pass optical rotation of Θ_{cw} and Θ_{ccw}

produce different polarization beating frequencies:

$$\omega_{cw} = \frac{\Theta_{cw}}{t_{rt}} = \frac{(\theta_F + \phi_c)\, c}{L} \tag{4.2a}$$

$$\omega_{ccw} = \frac{\Theta_{ccw}}{t_{rt}} = \frac{(\theta_F - \phi_c)\, c}{L} \tag{4.2b}$$

where $t_{rt} = L/c$ is the ring cavity roundtrip time and L is the ring cavity roundtrip length.

We notice that we can produce an extra pair of equations similar to (4.2). Changing the direction of the magnetic field B, the sign of the Faraday rotation angle θ_F changes so that the four beating frequencies can be written as:

$$\omega_{cw}(\pm B) = \frac{(\pm\theta_F + \phi_c)\, c}{L} + \omega_{noise}(t) \tag{4.3a}$$

$$\omega_{ccw}(\pm B) = \frac{(\pm\theta_F - \phi_c)\, c}{L} + \omega_{noise}(t) \tag{4.3b}$$

where we have added the term $\omega_{noise}(t)$, to include all nonideal, time-dependent offset and noise terms, such as from poor cavity alignment and from residual birefringence [11]. The term $\omega_{noise}(t)$ is supposed to be the same for both CW and CCW light beams.

By taking the difference of the absolute values of beating frequencies for each magnetic field direction we obtain:

$$\Delta\omega(+B) = |\omega_{cw}(+B)| - |\omega_{ccw}(+B)| = \frac{|\theta_F + \phi_c|\, c}{L} - \frac{|\theta_F - \phi_c|\, c}{L} = 2\phi_c \left(\frac{c}{L}\right) \tag{4.4a}$$

$$\Delta\omega(-B) = |\omega_{cw}(-B)| - |\omega_{ccw}(-B)| = \frac{|-\theta_F + \phi_c|\, c}{L} - \frac{|-\theta_F - \phi_c|\, c}{L} = -2\phi_c \left(\frac{c}{L}\right) \tag{4.4b}$$

where we assumed that $\theta_F > \phi_c$, as it is almost always the case.

Notice that the Faraday rotation θ_F cancels, as does the noise $\omega_{noise}(t)$ leaving only the desired term proportional to ϕ_c with a sign controlled by the sign of the B field. Hence, ϕ_c can be estimated without the need to reverse the magnetic field. However, if we combine equations (4.4a) and (4.4b) we obtain:

$$\Delta\omega(+B) - \Delta\omega(-B) = 4\phi_c \left(\frac{c}{L}\right) \tag{4.5}$$

Equation (4.5) can be written as:

$$\boxed{\phi_c = \left(\frac{L}{c}\right) \frac{\Delta\omega(+B) - \Delta\omega(-B)}{4}} \tag{4.6}$$

Expressing the angular frequency ω as $\omega = 2\pi f$, equation (4.6) can be written as:

$$\boxed{\phi_c = \frac{\pi}{2} \left(\frac{L}{c}\right) [\Delta f(+B) - \Delta f(-B)]} \tag{4.7}$$

Equations (4.4) and (4.5) demonstrate the strength of signal reversals, where two experimental signals, in principle, have everything in common except that the contribution

from the desired signal differs in sign. As a result, subtraction of the signals cancels all undesired components, while the desired signal is doubled, which gives the factor 2 in equations (4.4). The application of the second signal reversal gives a second factor of 2, and a total factor of 4, in equation (4.5).

These signal reversals allow the determination of ϕ_c without needing to remove the chiral sample, but simply by comparing the polarization beating frequencies of CW and CCW, as one direction provides a background reference for the other [11].

4.2 Mathematical Derivation of CRDP Equations

In this section we derive the equation for the CRDP signals using "Jones calculus" (appx. A).

We describe mirrors, M_i, with reflectivity R_i as:

$$J_{M_i}(R_i, \delta_i) = \sqrt{R_i} \begin{bmatrix} -e^{i\delta_i/2} & 0 \\ 0 & e^{-i\delta_i/2} \end{bmatrix} \tag{4.8}$$

Once again we assume almost normal incidence, meaning $\delta = 0$.

Chiral substances and Faraday rotators can be expressed as rotation matrices:

$$\mathcal{R}(\theta) = \begin{bmatrix} \cos(\theta) & -\sin(\theta) \\ \sin(\theta) & \cos(\theta) \end{bmatrix} \tag{4.9}$$

where θ represents the chiral angle or the Faraday angle. The different symmetry of chiral rotation and Faraday effect is enclosed in the sign of the angle.

For the CW beam the cavity (Figure 4.1) can be described as:

$$M_{cw}(\pm B) = J_{M_1}(R_1) J_{M_4}(R_4) \mathcal{R}(\pm\theta_F) J_{M_3}(R_3) J_{M_2}(R_2) \mathcal{R}(\phi) \tag{4.10}$$

Similarly for the CCW beam we have:

$$M_{ccw}(\pm B) = J_{M_1}(R_1) \mathcal{R}(-\phi) J_{M_2}(R_2) J_{M_3}(R_3) \mathcal{R}(\pm\theta_F) J_{M_4}(R_4) \tag{4.11}$$

After N roundtrips inside the cavity we have:

$$M^N_{cw}(\pm B) = R^{N/2}_{tot} \begin{bmatrix} \cos\left((\phi \pm \theta_F)\, N\right) & -\sin\left((\phi \pm \theta_F)\, N\right) \\ \sin\left((\phi \pm \theta_F)\, N\right) & \cos\left((\phi \pm \theta_F)\, N\right) \end{bmatrix} \tag{4.12}$$

and

$$M^N_{ccw}(\pm B) = R^{N/2}_{tot} \begin{bmatrix} \cos\left((-\phi \pm \theta_F)\, N\right) & -\sin\left((-\phi \pm \theta_F)\, N\right) \\ \sin\left((-\phi \pm \theta_F)\, N\right) & \cos\left((-\phi \pm \theta_F)\, N\right) \end{bmatrix} \tag{4.13}$$

where $R_{tot} \equiv R_1 R_2 R_3 R_4$. We assume that the light entering the cavity is lineraly polarized

with angle α with the x-axis:

$$P_i = \begin{bmatrix} \cos(\alpha) \\ \sin(\alpha) \end{bmatrix} \tag{4.14}$$

Furthermore, the transmission axis of the polarizer at the exit of the cavity is assumed to be on an angle χ with the x-axis. Hence, from Table A.2 we conclude that its matrix representation is:

$$J_{pol}(\chi) = \begin{bmatrix} \cos^2(\chi) & \cos(\chi)\sin(\chi) \\ \cos(\chi)\sin(\chi) & \sin^2(\chi) \end{bmatrix} \tag{4.15}$$

When the light passes through the cavity N times and emerges through the polarizer at the cavity exit, the final polarization we obtain is:

$$P_f^{cw} = J_{pol}(\chi) M_{cw}^N(\pm B) P_i \equiv \begin{bmatrix} a_f^{cw} \\ b_f^{cw} \end{bmatrix} \tag{4.16}$$

for the CW beam and

$$P_f^{ccw} = J_{pol}(\chi) M_{ccw}^N(\pm B) P_i \equiv \begin{bmatrix} a_f^{ccw} \\ b_f^{ccw} \end{bmatrix} \tag{4.17}$$

for the CCW.

The signal recorded by the photodiodes is:

$$I_f \propto |a_f|^2 + |b_f|^2 \tag{4.18}$$

From equations (4.16) and (4.17) we obtain:

$$I_f^{cw}(\pm B) = I_0 R_{tot}^N \cos^2\left[(\phi \pm \theta_F) N + (\alpha - \chi)\right] \tag{4.19}$$

$$I_f^{ccw}(\pm B) = I_0 R_{tot}^N \cos^2\left[(-\phi \pm \theta_F) N + (\alpha - \chi)\right] \tag{4.20}$$

where I_0 is a proportionality constant.

Since $R_{tot} \approx 1$ then R_{tot}^N can be written as:

$$R_{tot}^N = e^{N \ln(R_{tot})} \approx e^{-N(1-R_{tot})} \tag{4.21}$$

If we replace $N = t/t_{rt}$ and use equation (4.3) (with $\omega_{noise}(t) = 0$) we obtain:

$$\boxed{I(t) = I_0 e^{-t/\tau} \cos^2(\omega t + \xi)} \tag{4.22}$$

where $\tau = t_{rt}/(1 - R_{tot})$ is the ring-down time, and $\xi = (\alpha - \chi)$ is a constant phase term.

In Figure 4.2 a simulated CRDP signal is depicted as well as an exponentially decaying signal which we would obtain if there was no polarizer at the cavity exit.

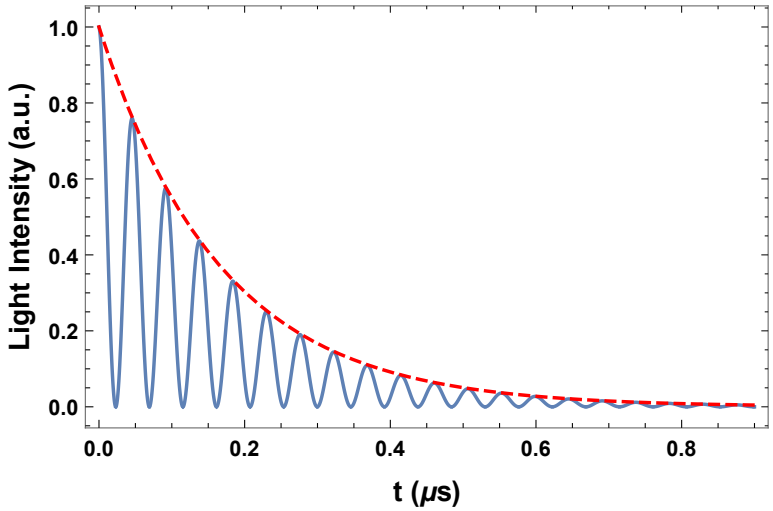

Figure 4.2: (Blue line) Simulation of a CRDP signal for the CW+ beam. We assumed mirror reflectivities $R_1 = R_2 = R_3 = R_4 = 0.997$, cavity length $L = 60$ cm, chiral angle $\phi = 1.8°$, faraday angle $\theta_F = 6°$, initial polarization $P_i = \begin{bmatrix} 1 \\ 0 \end{bmatrix}$ and the polarizer at the exit to be at $\chi = 0°$ with the x-axis. (Dashed line) The signal without the polarizer at the exit of the cavity.

4.3 Experimental Setup

The basics of the experimental setup we used for a signal-reversing CRDP bowtie cavity are shown in Figure 4.3.

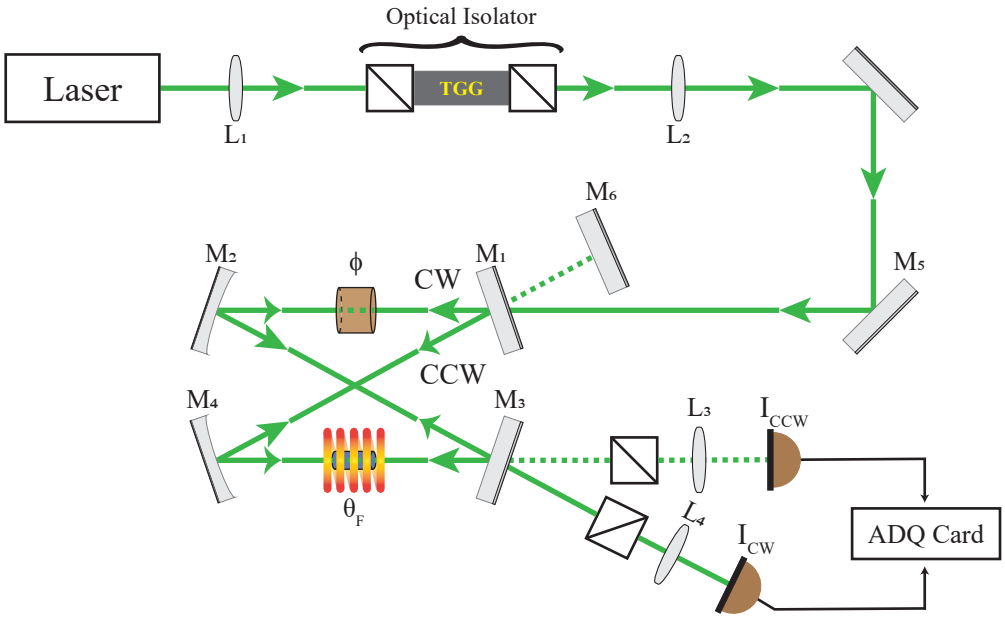

Figure 4.3: Experimental setup for CRDP with signal reversals. A pulsed laser at 532 nm with $\tau_{pulse} =$ 5.83 ns and a repetition rate 10 kHz is used. Before reaching the cavity, the beam passes through two lenses (L1, L2) and an optical isolator consisting of an anti-reflection coated TGG crystal. With M_6 the reflection on M_1 is retro-fed back into the cavity exciting the CCW mode. Inside the cavity, there is a chiral liquid sample inside a ≈ 40 μl cell creating an angle ϕ. The faraday angle θ_F is produced by a 7mm long CeF_3 crystal inside a coil producing a magnetic field of ≈ 1000 G. CW and CCW beams pass through polarizing beam splitters and are focused on two Si photodiodes. The signal of the photodiodes is recorded and analyzed by a data acquisition card.

Before the light reaches the cavity entrance, it passes through an optical isolator configuration consisting of an anti-reflection coated TGG crystal inside a constant magnetic field with two polarizers rotated as indicated in Section 2.5. That way we ensure that light from the rest of the optical system does not reach the laser causing unexpected damage. Moreover, light is spatially modified to match the cavity's geometrical characteristics, by two thin lenses L_1 and L_2 with $f_1 = 1000$ mm and $f_2 = 500$ mm respectively.

The bowtie ring cavity we use has plenty of advantages compared to the conventional ring cavities. In bowtie cavities the angle of incidence (AOI) at the mirrors is small ($< 5°$) which not only allows the birefringence at each reflection to be small but also it lets us use $0°$ AOI mirrors which are the same mirrors for linear cavities. In contrast, conventional ring cavities with $45°$ AOI, have several drawbacks. The birefringence at each reflection can be very large, the cavity lifetime is typically very different for s and p polarization modes and the circular birefringence from one of the four mirrors being out of plane (appx. B) is much bigger than that for a bowtie cavity [11].

The ring-down cavity had a total length of 3.61 m ($t_{rt} \approx 12$ ns) and comprised four highly reflective mirrors. Specifically, the cavity consists of two laser mirrors (mirror M_2 and M_4) with reflectivity $R \approx 99.98\%$ and a radius of curvature 1m as well as a plane input coupler (mirror M_1) with $R \approx 99.9\%$ and a plane output coupler (mirror M_3) with $R \approx 99.8\%$. All mirrors were manufactured to maximally reflect at 532 nm by Layertec GmbH. It is worth mentioning that the two couplers have different reflectivities because there is a trade-off between high ring-down time, which increases for higher R, and light intensity, which increases with lower R.

The experiment was performed with a Q-switched pulsed laser system at 532nm (Roither RLTMPL-532-500-3-19042759). Specifically, the laser pulses had an average power of 554 mW at a repetition rate of 10 kHz, pulse duration $\tau_{pulse} \approx 5.83$ ns, and a nearly TEM_{00} transverse mode (appx. C).

The large Faraday rotation, θ_F, was induced using the Faraday effect of an intra-cavity, anti-reflection coated CeF_3 magneto-optic crystal 7 mm long with a diameter of 4 mm. The CeF_3 has a high Verdet constant at 532 nm approximately equal to 190 rad T^{-1} m^{-1}.

The crystal is placed along the axis of an in-house-built, water-cooled coil. A custom, programmable, high-power electronics scheme was employed which allowed inverting the direction of the magnetic field at a repetition rate that can be varied between 0.5 and 100 Hz. Specifically, a very stable current source (Delta Elektronika SM 52-30) was connected to the coils of the electromagnet through an inverting relay from CAMTEC. The reversal of the magnetic field was possible by reversing the polarity of the connections to the coils, and the logic of the circuit was controlled through an Arduino-Uno microcontroller board. The current supplied to the coil was 10 A, producing a magnetic field of approximately 1,000 G, which, in turn, yields enough polarization beatings within the ring-down time to make the precise calculation of the polarization beating frequency possible.

The samples were placed in a 3 mm thick cell with a diameter of 4 mm, yielding a cell with a sample volume of 40 μl (Figure 4.4). The cell is terminated by two windows held

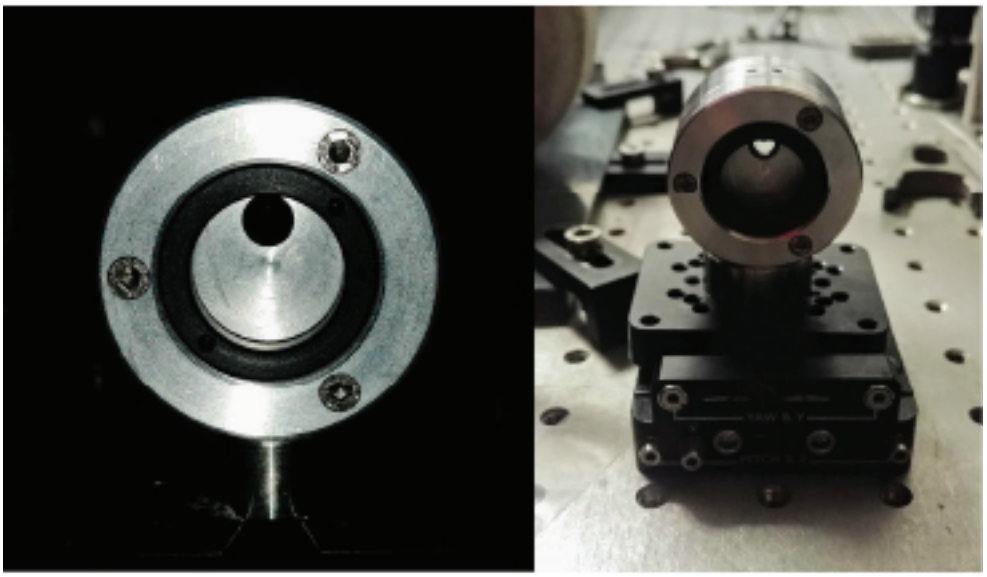

Figure 4.4: Single-drop cell of 3 mm thickness and 4 mm diameter. In the second picture the cell is shown on a rotation stage manufactured by THORLABS.

in place by a threaded system, which distributes pressure evenly on the window so as to avoid stress-induced birefringence. The windows used were nano-texture windows from Newport which provide broadband operation. The whole system was placed on a rotation stage allowing precise movement of the cell on all three axes.

The linearly polarized 532 nm laser beam is injected into the cavity via mirror M_1 to excite the CW cavity mode and the reflection is retro-fed back into the cavity again from mirror M_1 to excite the CCW mode. The CW and CCW modes simultaneously sample the CeF_3 crystal and the chiral sample and leak out of the cavity from all four mirrors, but at a much higher rate from the output coupler. For that reason, mirror M_3 with the highest transmission coefficient was used as an output mirror so that the cavity ring-down trace could be detected.

Cube polarizing beam splitters were used for the analysis of the polarization state of the output beams. The analyzers were positioned on rotation mounts, with their transmission axes almost parallel to the respective input polarization. Short lenses, L_3 and L_4, with $f = 35$ mm were used to focus the emerging radiation on two biased Si photodiodes (Thorlabs DET10A).

The signals are recorded by a dedicated, high-bandwidth data acquisition card (Teledyne ADQ14DC-2X PCIe | 14-bit | dual-channel 2 GS/s per channel | 2Gb RAM | Kintex 7 FPGA). The card is utilized with a software developed by PHOTEK. The software is operated via a GUI (Graphical User Interface), and can digitize and store in memory the signals from all pulses for both channels. The software also controls the reversal of the magnetic field by communicating with the Arduino-Uno referred above. Furthermore, it automatically averages the recorded data, per channel, per magnetic field orientation, applies the fitting algorithms, and outputs two spreadsheet files, one with all fitted parameter values, and one with the reversal calculations performed.

4.4 Measurement of Single-drop Solutions

Some typical signals we obtain using our pulsed CRDP apparatus are shown in Figure 4.5. The signals depicted represent the polarization beating of the CW and the CCW propagation beams for the same direction of the magnetic field. The CCW mode has lower amplitude since it is retro-fed back inside the cavity and as a result light is lost in the reflection-transmission procedure.

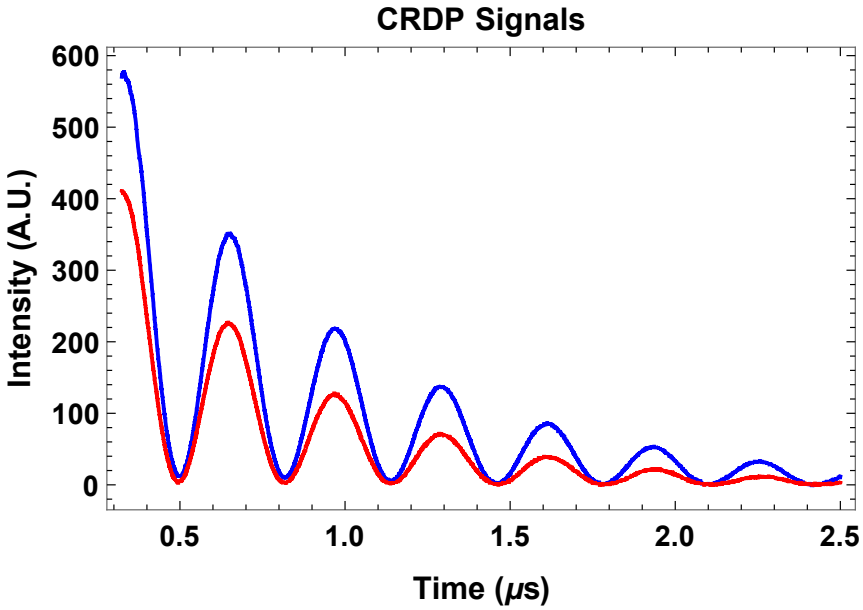

Figure 4.5: Experimental trace from the output of the CRDP apparatus. The blue line represents the signal for the CW+ beam. The red line represents the signal for the CCW+ beam.

For each experimental measurement, the CW and CCW modes are recorded and the frequency of the oscillation is extracted by a time-domain fitting which is performed by the data acquisition card described in Section 4.3.

The signals are ideally expressed by equation (4.22) as explained in detail in Section 4.2. However, actual signals and the ideal model slightly differ. The first factor that causes the signal to diverge from the ideal model is spurious linear birefringence in the cavity. Linear birefringence slightly changes the linearly polarized light inserting the cavity, turning it into elliptically polarized and leading to reduction of the modulation depth of the signal. In addition, the signal's baseline may not be equal to zero due to offsets introduced by the detection electronics (e.g. photodiodes). To account for these effects, the function we fitted on the data was:

$$I(t) = I_0 \; e^{-t/\tau} \left[\cos^2\left(2\pi f t + \xi\right) + C_1\right] + C_2 \tag{4.23}$$

where C_1 accounts for experimental imperfections that reduce the modulation depth of the polarization beating and C_2 is a global signal offset. Estimating the four frequencies, $f_{cw}^{\pm}$ and $f_{ccw}^{\pm}$, allows us to determine the chiral angle ϕ using equation (4.7).

4.4.1 Preliminary Measurements

To establish baseline operation, we first took measurements of the empty cavity. In Figure 4.6(a), we see the measured variance in rotation angles for a series of individual 200 ms measurements, and for a total measurement time of 50 seconds (that is, 250 measurements in total). Each measurement consists of one magnetic field reversal (100 ms of $+\mathbf{B}$, followed by 100ms of $-\mathbf{B}$), and, for each direction of the magnetic field, we acquire, average, and perform the decaying sinusoidal fit equation (4.23) to the signal produced by 1,000 incoming pulses, both for the CW and CCW beams. In reality, each measurement is a few tens of milli-seconds longer, as we allow the magnetic field to settle after reversing direction.

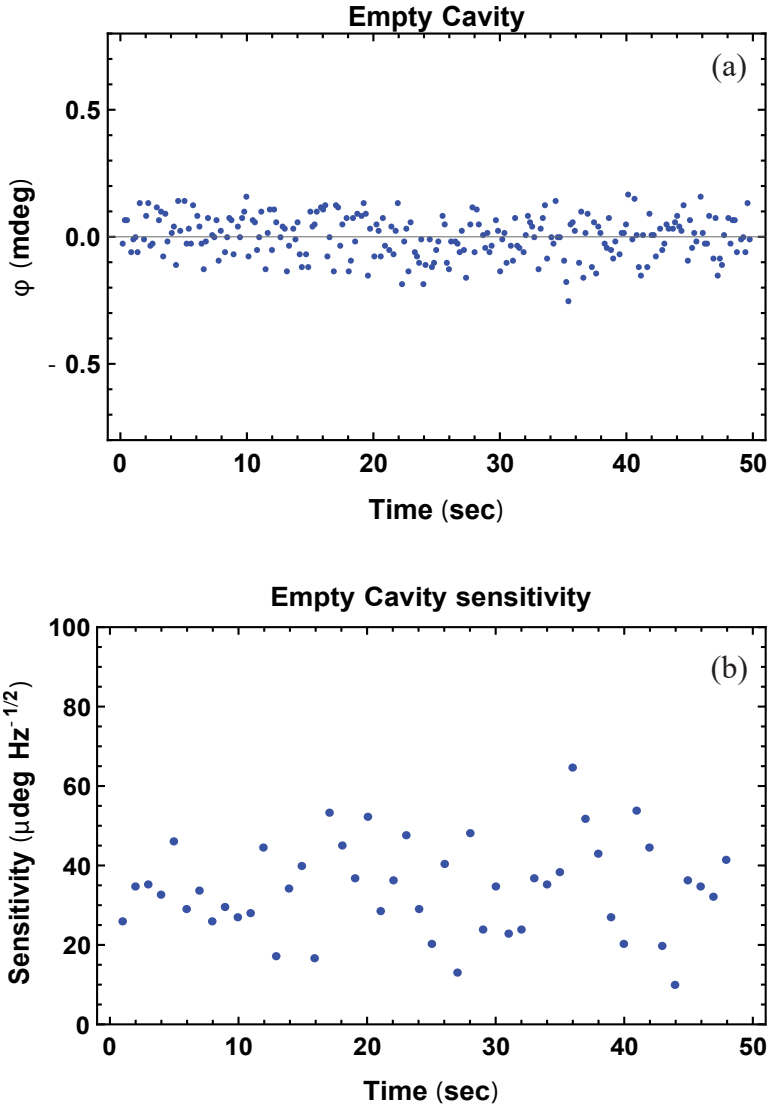

Figure 4.6: Empty cavity. (a) A set of 250 optical rotation measurements for the empty cavity. Each measurement lasts 200 ms and consists of one B-field reversal. For each B-field direction, 1,000 pulses are measured, averaged, and fitted for both the CW and CCW channels. The rotation angle value is calculated via the workflow described above in the text. This is a typical set of measurements yielding a standard deviation of $\sigma = 81$ μdeg. (b) The measurements of (a) were grouped and averaged in one-second intervals, and their variance was divided by the square root of the number of measurements per second ($/\sqrt{5}$). Thus, the empty cavity sensitivity in PSD units is found to be $\delta\phi = 34$ $\mu\text{deg}/\sqrt{\text{Hz}}$.

From this set of measurements, we calculate the standard deviation of the rotation variance for the empty cavity to be $\sigma = 81$ μdeg. Obviously, the mean rotation angle for the empty cavity is zero.

In Figure 4.6(b) we group the measurements of Figure 4.6(a) in one-second intervals, and we calculate the sensitivity in spectral density units, where it is worth noting that we have established independently that the mean values of fitted parameters follow a normal distribution, and we are thus allowed to scale the sensitivity with the square root of the measurement time. From this calculation, we obtain an empty-cavity sensitivity of approximately $\delta\phi = 34$ μdeg/$\sqrt{\text{Hz}}$.

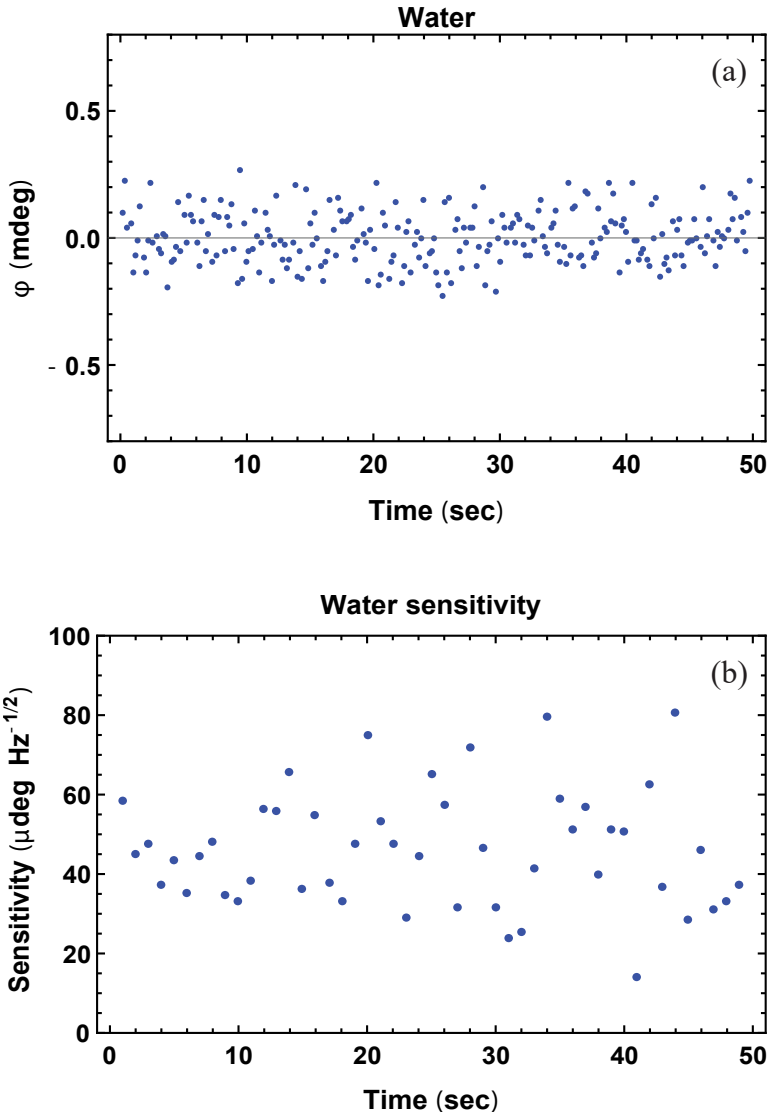

Figure 4.7: Water. (a) As in Figure 4.6, a set of 250 optical rotation measurements, for a pure water sample this time, yields a zero mean optical rotation value and a standard deviation of $\sigma = 101$ μdeg. (b) Grouping the uppermost measurements we calculate the sensitivity for a water sample, in PSD units, $\delta\phi = 47$ μdeg/$\sqrt{\text{Hz}}$.

Having established baseline operation, we performed the same measurements for pure water as the sample, since the water was the main solvent we used throughout our measurement sets. A typical measurement run is shown in Figure 4.7, where the optical

rotation variance and sensitivity are calculated as before to be: $\sigma = 101$ μdeg and $\delta\phi = 47$ $\mu\text{deg}/\sqrt{\text{Hz}}$. We notice that the introduction of the liquid sample in the cavity does not lead to a very significant deterioration of sensitivity.

4.4.2 Lysozyme

We followed up with measurements of lysozyme for various concentrations. Lysozyme is an enzyme found in secretions of animals and humans such as tears, sweat and saliva. It is part of the innate immune system, having antibacterial effects. For example, it eliminates bacteria found in tears, and therefore its abundance in tears is a sign of a healthy eye. Low levels of lysozyme can indicate bacterial infections caused by dry eye syndrome. The precise measurements of lysozyme in tears can thus provide a diagnostic tool about the eye's health [24].

The results are displayed in Figure 4.8, where each data point comes from measurements similar to those of Figures 4.6 and 4.7.

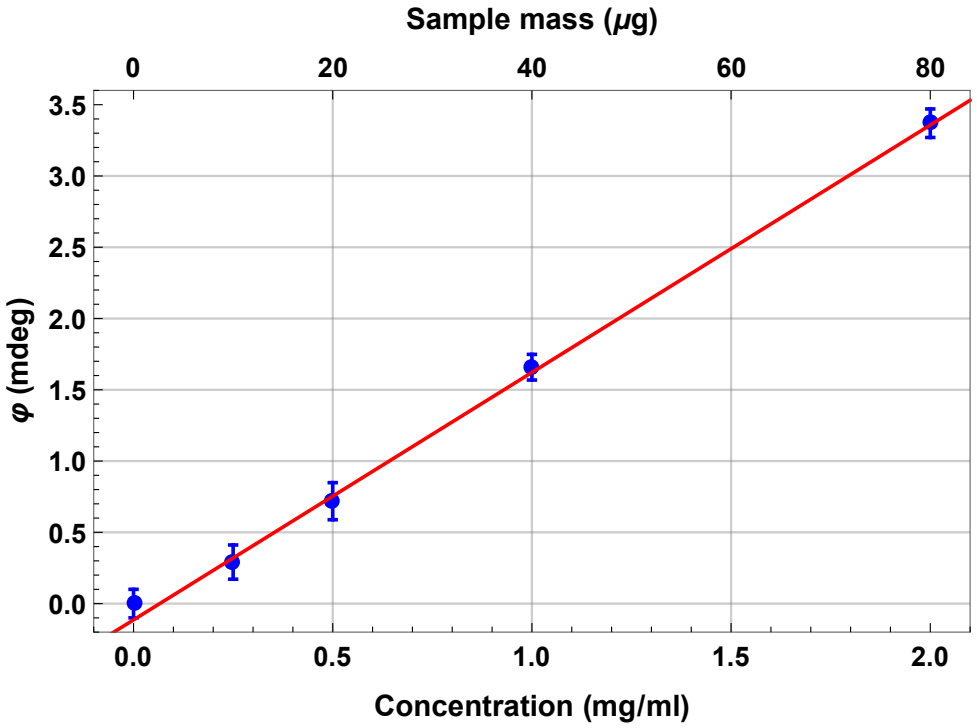

Figure 4.8: Optical rotation measurements vs concentration, for the determination of the specific rotation of the lysozyme. Each point represents the mean value of 250 measurements as those depicted in Figure 4.6(a) and 4.7(a). Errorbars are the 1σ value of every mean value. Typical dataset optical rotation variance, σ_ϕ=130 μdeg, computed instrument sensitivity, $\delta\phi = 60$ $\mu\text{deg}/\sqrt{\text{Hz}}$, calculated specific rotation, $\alpha^{[532nm]} = 69 \pm 2$ deg dm^{-1} g^{-1} ml.

The extracted value for the specific rotation of lysozyme at 532 nm we estimated, using (2.14), is $\alpha^{[532nm]} = 69 \pm 2$ deg dm^{-1} g^{-1} ml, which is in agreement with [24].

4.4.3 Tears

After measuring pure lysozyme, we tried to measure the chiral rotation of actual human tears. Specifically, in collaboration with the Medical department of University of Crete (Prof. Tsilimparis and Dr. Tsoka) we collected enough quantity of tears, $\approx$ 200 μl, to proceed with the measurement. In order to avoid contamination of the sample, the collection procedure followed was extremely thorough. The tears were directly extracted from the eye with a micro-pipette and stored in separate containers for each donor, avoiding mixing.

Unfortunately, the sample behaviour was not the one expected. Although human tears consists of 98% water, the samples showed an oily composition. This is probably due to substances such as lipids that prevent water from evaporating and also keep the tear's surface smooth so that we can see through it.

As a result, the traces obtained, depicted in Figure 4.9, had small ring-down times, compared with water signals, leading to signals with not enough polarization beatings. The lysozyme estimated was 0.67 ± 0.17 mg/ml while for a healthy person is approximately 1.4 mg/ml. As far as we know, the tears donated by a healthy individual and as a result we conclude that this discrepancy is the outcome of poor signal quality.

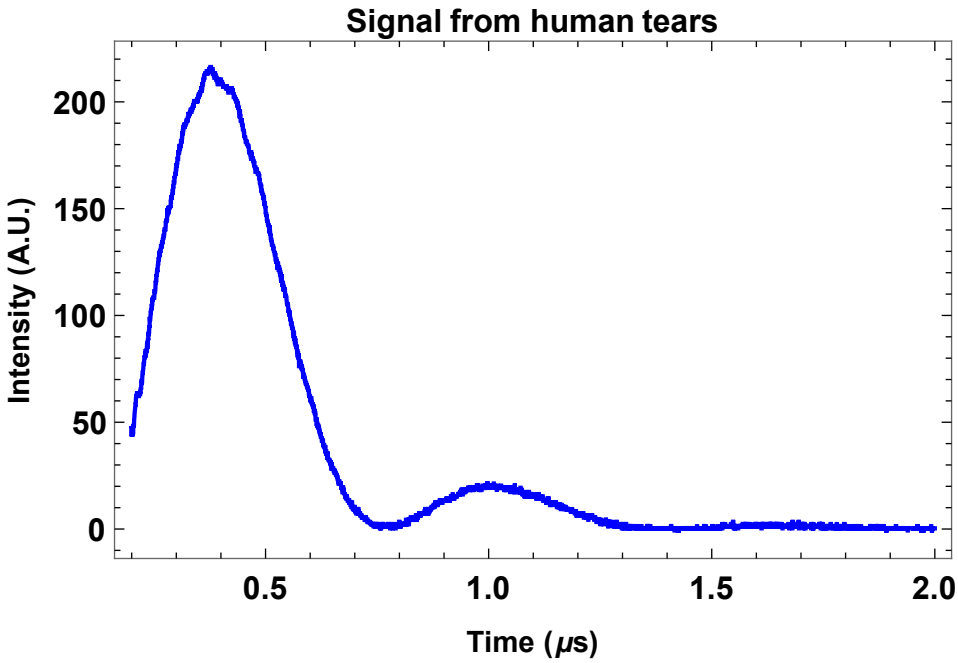

Figure 4.9: Experimental trace from the output of the CRDP apparatus containing human tears. The trace represents the polarization beating of the CW- propagation beam passing through human tears diluted five times in water.

Chiral measurements of human tears are depicted in Figure 4.10.

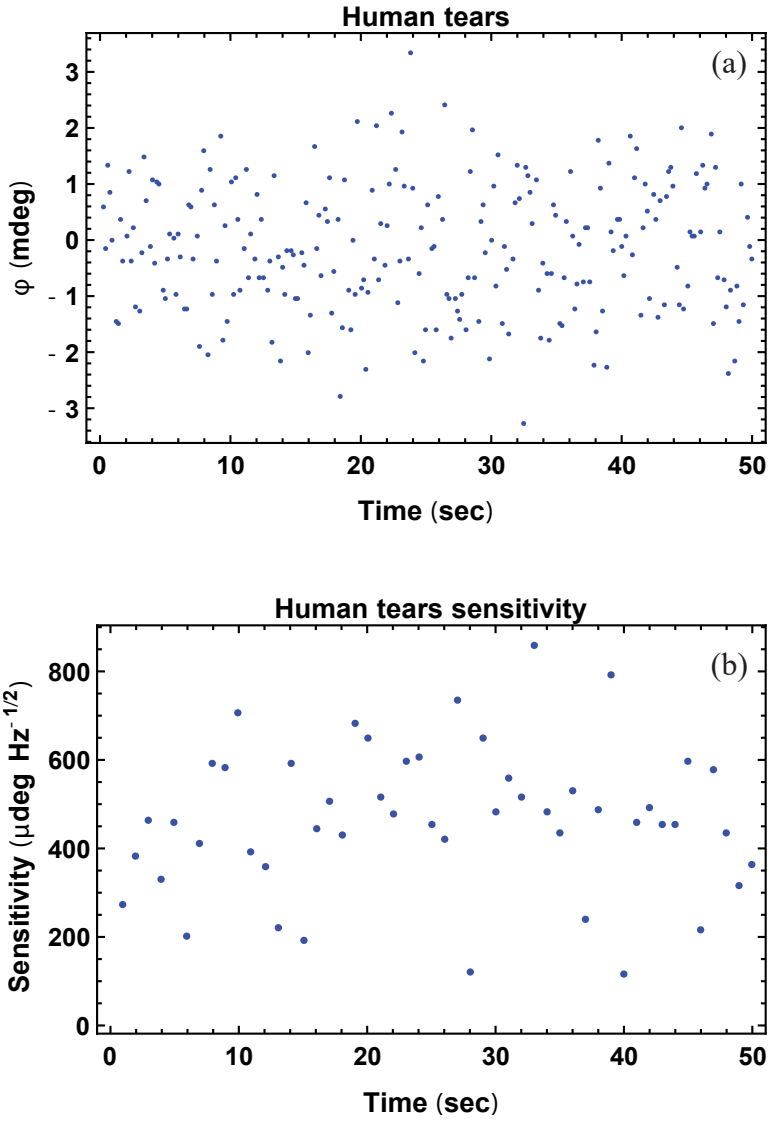

Figure 4.10: Human tears. (a) As in Figure 4.6(a) and 4.7(a), a set of 250 optical rotation measurements, for tears sample diluted five times in water, yields a mean optical rotation value of -0.14 mdeg and a standard deviation of $\sigma = 1.1$ mdeg. (b) Grouping the uppermost measurements we calculate the sensitivity of the sample, in PSD units, $\delta\phi = 466\ \mu\text{deg}/\sqrt{\text{Hz}}$.

Next, we measured artificial tears ("TEARS NATURABLE FREE MED" by Novartis) containing chiral substances such as Dextran 70. In Figure 4.11 the optical rotation is depicted as a function of artificial tears' concentration. For the measurement of 50 % concentration, artificial tears were diluted in water. We note that we cannot extract a value for the specific rotation since the exact mass of the chiral substances inside the tears were not given by the drug manufacturer. Nevertheless, the fact that we obtain a straight line clarifies that artificial tears can be measured.

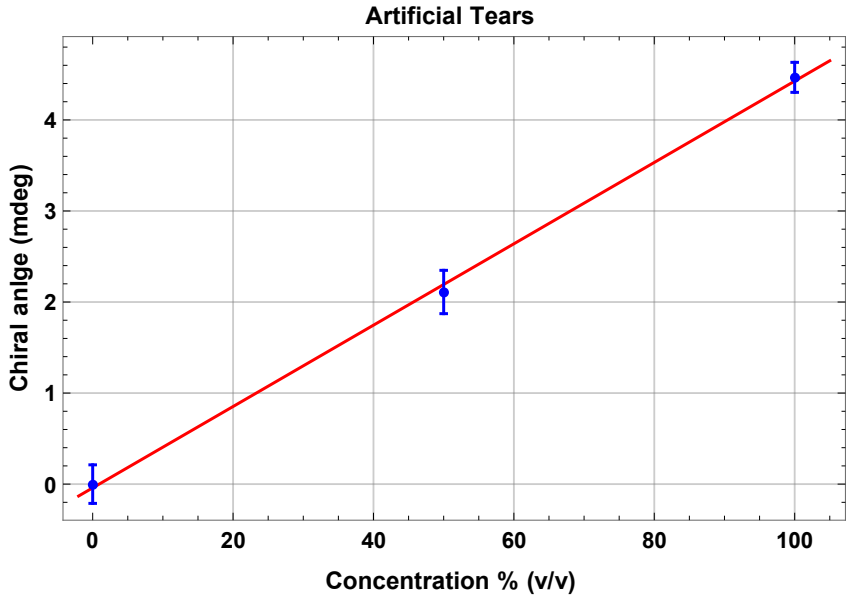

Figure 4.11: Optical rotation measurements vs concentration for artificial tears. Each point represents the mean value of 250 measurements as those depicted in Figure 4.6(a) and 4.7(a). Errorbars are the 1σ value of every mean value. For the measurement of 50 % concentration, artificial tears were diluted in water.

4.4.4 Tartaric Acid

The next chiral substance we measured was L(+)-tartaric acid. Tartaric acid is an organic substance that occurs naturally in various plants, fruits, and wine. It plays a central role in the food industry where it is used as an additive and flavoring agent. It is also employed in industries such as ceramics, textile printing, tanning, photography, and pharmaceuticals.

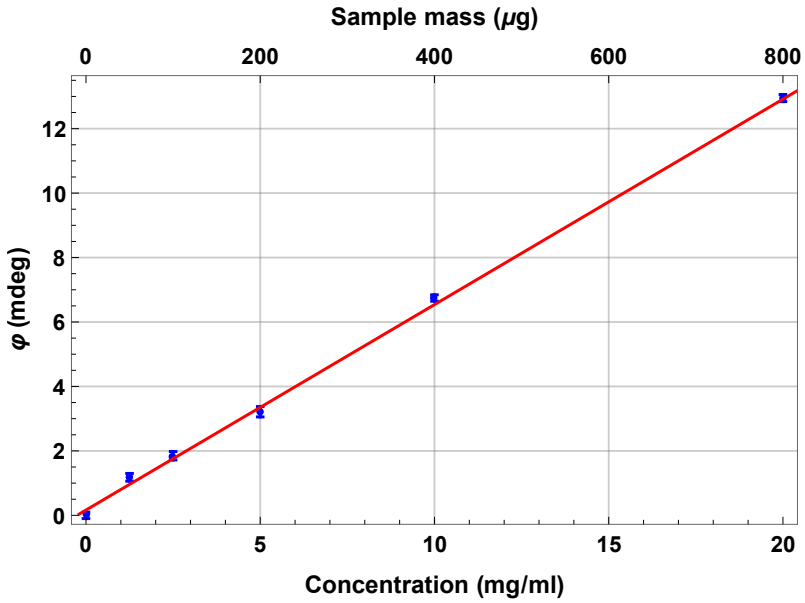

Figure 4.12: Optical rotation measurements vs concentration, for the determination of the specific rotation of the tartaric acid. Each point represents the mean value of 250 measurements as those depicted in Figures 4.6(a) and 4.7(a). Errorbars are the 1σ value of every mean value. .Typical dataset optical rotation variance σ_ϕ=110 μdeg, computed instrument sensitivity, $\delta\phi = 50$ μdeg/$\sqrt{\text{Hz}}$, calculated specific rotation, $\alpha^{[532nm]} = 25 \pm 1$ deg dm^{-1} g^{-1} ml.

The results are shown in Figure 4.12. The extracted value for the specific rotation of tartaric acid at 532 nm we estimated is $\alpha^{[532nm]} = 25 \pm 1$ deg dm^{-1} g^{-1} ml.

4.5 Discussion

At this point, it should be emphasized that the current work is based on an idea initially conceived and implemented by 'Polarization Spectroscopy" group at FORTH, starting approximately ten years ago [1, 11, 24–26]. The configuration described here provides groundbreaking results that compete with the top-of-the-line commercial polarimeters, summarized in Table 4.1.

The optical rotation sensitivity limit of commercial polarimeters is typically of order 1 mdeg, with the best polarimeters reaching down to 0.3 mdeg, for a 10 cm cell and for measurement times of a few seconds. The current apparatus surpass commercial polarimeters by providing tangible improvements to all their current limits: sensitivity, time resolution, and sample volumes.

Starting with the sample volumes, in commercial polarimeters sample volumes are much larger than those described here. Specifically, sample volumes are typically in the range of 0.5 to 15 ml, which is quite disadvantageous for rare or expensive samples, or samples that are only available in small volumes, e.g. human tear samples. With our current setup, we have already reduced absolute sample volumes by at least one order of magnitude using our ≈ 40 μl cell, described briefly in Section 4.3. Hence, it is shown that chiral sensing in the micro-liter regime is possible.

As far as sensitivity is concerned, typical sensitivities of commercial polarimeters are of the order of 5 mdeg/$\sqrt{\text{Hz}}$. Our cavity setup has proven to reach sensitivities below 50 μdeg/$\sqrt{\text{Hz}}$, when the chiral sample properties do not render the apparatus inoperable. This is mainly due to the implementation of signal-reversals that enable rapid background subtractions, which, in turn, result in reduced common mode noise levels and ultimately provide high Signal-to-Noise Ratios and better sensitivities. Moreover, the usage of the Fast DAQ Card and the way we reverse the magnetic field, described in Section 4.3, played a major role in further improving sensitivity. Specifically, although oscilloscopes have high enough bandwidth to digitize the incoming signal, they can not trigger and store data at every incoming pulse, due to the combination of slow data processing by the built-in software and the high repetition rate of the laser (10kHz). This leads to a loss of ring-down information for about 99% of the incoming pulses. However, the Fast DAQ Card captures every pulse leading to significant sensitivity improvement. Furthermore, the all-DC inverting relay scheme we implement to reverse the magnetic field, provides a constant current to the coil, rather than a constant voltage, leading to significantly reduced noise levels.

A consequence of our ability to measure single-drop solutions with high sensitivity is that the minimum quantity of the chiral substance required to determine its specific rotation, is significantly smaller than in commercial polarimeters. For example, in the

case of lysozyme (Figure 4.8) 10 μg were enough for the determination of α, whereas approximately 10 mg would be needed in a typical commercial instrument.

Although our apparatus seems to produce some remarkable results, there is still room for improvement. As one can observe in Figures 4.8, 4.11 and 4.12 some points diverge from the straight line. The main reason for this discrepancy is temperature effects mainly associated with the cell. Specifically, we noticed that the longer we waited for the samples inside the cell to settle, the less the variance of the chiral angles was with time. We believe that if we apply technology similar to that used for the manufacture of temperature stabilized cells the configuration will be less dependent on thermal drifts.

Furthermore, possible spurious noise sources such as air fluctuations and vibrations can be canceled out with a sealed, vibration-compensating cavity design that will minimize the effect of the external environment.

In addition, the sensitivity can be improved by using higher quality optics coatings, leading to longer ring-down times as well as by increasing the number of pulses per second using a higher repetition rate laser source.

	Rudolph Autopol VI	CRDP	Improvement
Sensitivity $\left(\mu\text{deg}/\sqrt{\text{Hz}}\right)$	5000	50	$\times$ 100
Absolute Sample Value	0.5-15 ml	< 50 μl	$\times$ 10 - 300
Min. quantity for α determination	10 mg	0.01 mg	$\times$ 1000

Table 4.1: Comparison of our CRDP apparatus with the best commercial polarimeter manufactured by Rudolph Search Analytical (`https://rudolphresearch.com/products/polarimeters/autopol-vi/`)

Appendices

Appendix A

Polarization of Light

When the electric field vector **E** of light maintains a constant direction of oscillation, or it varies spatially in a regular manner then light is said to be polarized. The polarization of light is related to the transverse character of electromagnetic radiation. In 1941 R. Clark Jones [27] proposed a matrix technique to describe polarized light[1]. According to Jones, polarized light can be represented by two-element column vectors (Jones Vectors) and as a result, optical elements that modify the state of polarization can be represented by 2×2 matrices. Here, we present the most essential parts of the theory of light polarization based on the book by Pedrotti et.al, *Introduction to Optics* [28].

A.1 Jones Vectors

Without loss of generality, we consider a ray of light directed along the $+z$ axis in vacuum. Since the ray travels along the +z direction, the electric field **E** will be along xy plane.

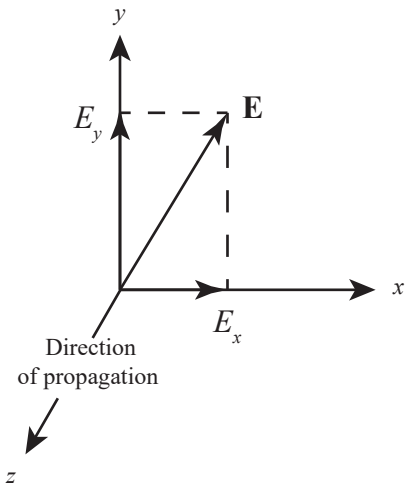

Figure A.1: Representation of the instantaneous **E** traveling in the $+z$ direction.

[1] "Jones calculus" is applied only on polarized light. In 1943 Hans Mueller developed a matrix technique known as "Mueller calculus" that can describe both polarized and "unpolarized" light and is based on 4×4 matrices.

In terms of the unit vectors $\hat{\mathbf{x}}$ and $\hat{\mathbf{y}}$:

$$\mathbf{E} = E_x\hat{\mathbf{x}} + E_y\hat{\mathbf{y}} \tag{A.1}$$

Assuming that each component is a plane wave, they can be written as:

$$E_x = E_{0x}e^{i(kz-\omega t+\phi_x)} \tag{A.2}$$

and

$$E_y = E_{0y}e^{i(kz-\omega t+\phi_y)} \tag{A.3}$$

combining (A.1) - (A.3) we obtain:

$$\mathbf{E} = \left[E_{0x}e^{i\phi_x}\hat{\mathbf{x}} + E_{0y}e^{i\phi_y}\hat{\mathbf{y}}\right]e^{i(kz-\omega t)} = \tilde{\mathbf{E}}_{\mathbf{0}}e^{i(kz-\omega t)} \tag{A.4}$$

where $\tilde{\mathbf{E}}_{\mathbf{0}}$ is the complex amplitude.

According to (A.4) the state of polarization is totally determined by the terms inside the brackets, the complex amplitude. The bracketed quantity, written as a two-element column vector, is known as Jones Vector:

$$\tilde{\mathbf{E}}_{\mathbf{0}} = \begin{bmatrix}\tilde{E}_{0x}\\ \tilde{E}_{0y}\end{bmatrix} = \begin{bmatrix}E_{0x}e^{i\phi_x}\\ E_{0y}e^{i\phi_y}\end{bmatrix} \tag{A.5}$$

It is a common practice to normalize Jones vectors:

$$\tilde{\mathbf{E}}_{\mathbf{0}} = \begin{bmatrix}\tilde{E}_{0x}\\ \tilde{E}_{0y}\end{bmatrix} \rightarrow \frac{1}{\sqrt{|\tilde{E}_{0x}|^2 + |\tilde{E}_{0y}|^2}}\begin{bmatrix}\tilde{E}_{0x}\\ \tilde{E}_{0y}\end{bmatrix} \tag{A.6}$$

Every kind of polarization can be described from the values of E_{0x}, ϕ_x, E_{0y} and ϕ_y. Table A.1 provides a summary of the most common Jones vectors. It must be emphasized that Jones vectors are not unique. If multiplied by a real constant, the state of polarization remains the same contrary to the amplitude that changes.

It is worth noting that if E_x leads E_y, then $\phi_y > \phi_x$, a result opposed to intuition. This contradiction arises from our choice of phase in the formulation of $\mathbf{E}$ at (A.2) and (A.3) where the time dependent term in the exponent was chosen to be negative [28].

Type of Polarization	$\Delta\phi = \phi_y - \phi_x$	**Jones Vector**
Vertical	$m\pi,\ m \in \mathbb{Z}$	$\begin{bmatrix} 0 \\ 1 \end{bmatrix}$
Horizontal	$m\pi,\ m \in \mathbb{Z}$	$\begin{bmatrix} 1 \\ 0 \end{bmatrix}$
Linear with inclination α with x-axis	$m\pi,\ m \in \mathbb{Z}$	$\begin{bmatrix} \cos(\alpha) \\ \sin(\alpha) \end{bmatrix}$
Left Circular	$\frac{\pi}{2}$	$\frac{1}{\sqrt{2}} \begin{bmatrix} 1 \\ i \end{bmatrix}$
Right Circular	$-\frac{\pi}{2}$	$\frac{1}{\sqrt{2}} \begin{bmatrix} 1 \\ -i \end{bmatrix}$
Left Elliptical	$(m + \frac{1}{2})\pi,\ m \in \mathbb{Z}$	$\frac{1}{\sqrt{A^2 + B^2}} \begin{bmatrix} A \\ iB \end{bmatrix}$
Right Elliptical	$(m + \frac{1}{2})\pi,\ m \in \mathbb{Z}$	$\frac{1}{\sqrt{A^2 + B^2}} \begin{bmatrix} A \\ -iB \end{bmatrix}$
Left Elliptical	$\neq \begin{cases} m\pi \\ (m + \frac{1}{2})\pi \end{cases},\ m \in \mathbb{Z}$	$\frac{1}{\sqrt{A^2 + B^2 + C^2}} \begin{bmatrix} A \\ B + iC \end{bmatrix}$
Right Elliptical	$\neq \begin{cases} m\pi \\ (m + \frac{1}{2})\pi \end{cases},\ m \in \mathbb{Z}$	$\frac{1}{\sqrt{A^2 + B^2 + C^2}} \begin{bmatrix} A \\ B - iC \end{bmatrix}$

Table A.1: Normalized Jones Vectors

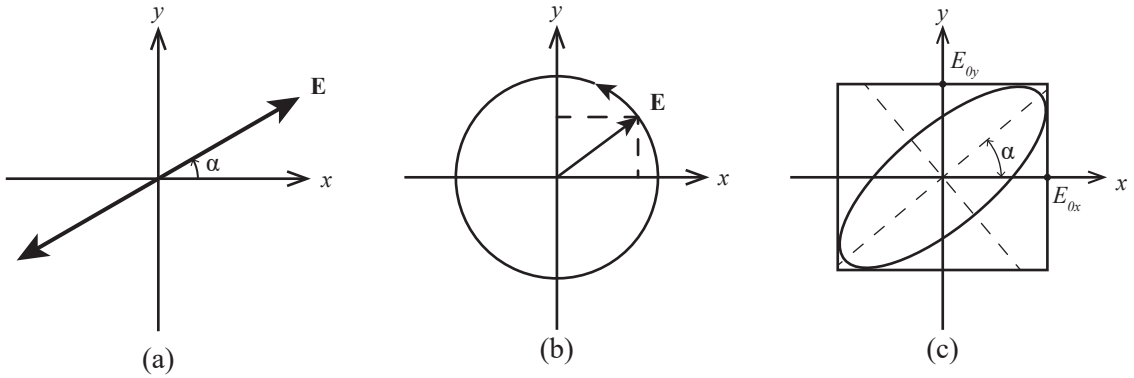

Figure A.2: Different types of polarization. (a) Linearly polarized light with angle α with x-axis. (b) Left circularly polarized light. (c) Elliptically polarized light.

A.2 Matrix Representation of Optical Elements

Since light is described as a two-element column vector it follows naturally that optical elements which modify the state of polarization will be 2×2 matrices. The final polarization state of light emerging from any kind of configuration, P_f, can be evaluated by subjecting the initial polarization vector, P_i , to the sequence of transformations, J_{tot}, generated by passage through individual optical elements:

$$P_f = (J_N J_{N-1} \dots J_2 J_1)\, P_i = J_{tot} P_i \tag{A.7}$$

We note that this kind of treatment neglects changes in spatial characteristics [22]. Here, we briefly present the operation of the most commonly used optical components.

Linear Polarizer

A linear polarizer is an optical element that selectively allows $\vec{\mathbf{E}}$ - vibrations to be transmitted in a given direction, while removing all (ideally) of the vibrations in the perpendicular direction. In real-life conditions, linear polarizers are not exactly 100% efficient, so the transmitted light is partially polarized. In Figure A.3 the operation of a linear polarizer is schematically presented. Unpolarized light traveling in the z-direction passes through a linear polarizer, whose transmission axis (TA) is vertical. As it is illustrated below, the light transmitted includes components only along the TA direction and is therefore linearly polarized in the vertical direction. In the figure, the process is assumed to be totally efficient and as a result, the horizontal components of the original light have been removed.

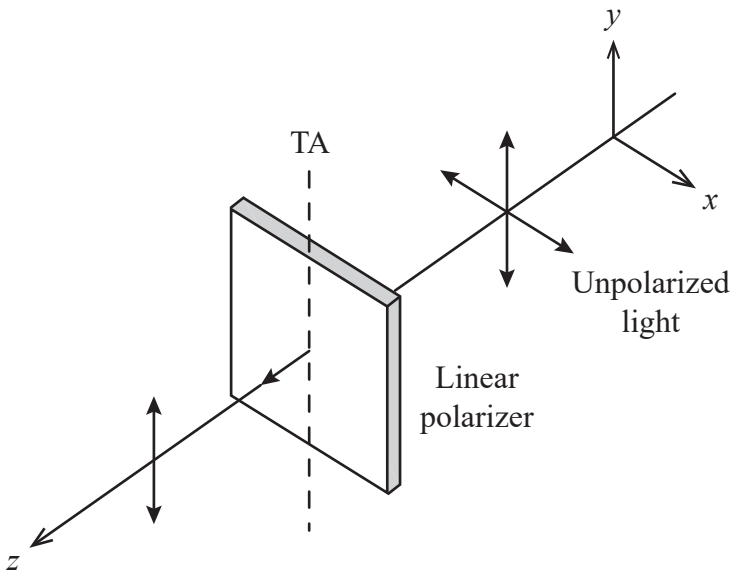

Figure A.3: Operation of a linear polarizer. Unpolarized light turns into vertically polarized after passing through a linear polarizer with a vertically oriented transmission axis (TA).

Phase Retarder

In contrast to the linear polarizer, the phase retarder does not remove either of the orthogonal components of $\vec{\mathbf{E}}$-vibrations, but rather, introduces a phase difference between them. When light corresponding to each orthogonal component travels with a different speed through such an optical element, then there will be a cumulative phase difference $\Delta\phi$ between the two waves as they emerge. The different speeds usually occur due to different rates of absorption for each component along a given axis. When we refer to phase retarders we refer to the fast axis (FA) and slow axis (SA) directions. Components along the FA travel faster than the components along the SA. When the net phase difference $\Delta\phi = \pi/2$, the retardation plate is called a **quarter-wave plate**, while when it is π, it is called a **half-wave plate**.

It is worth mentioning that quarter-wave plates transform circularly polarized light into linearly polarized. The opposite is also true when the linearly polarized light has its two orthogonal components equal in magnitude. Furthermore, the half-wave plate is usually used to rotate the plane of linearly polarized light. Specifically, when the polarization plane of light is at an angle θ with the FA of the half-wave plate, then the light emerging through the optical element is rotated by 2θ compared to its initial orientation.

Table A.2 contains the Jones matrices of the most commonly used optical elements. Table A.3 describes the physical processes of light reflecting from a mirror surface, passing through a chiral substance, and experiencing linear birefringence. It is worth mentioning that chirality is a rotation matrix that rotates linearly polarized light by a chiral angle θ_{cr}.

Optical Element	Jones Matrix
Rotator by angle θ	$\mathcal{R}(\theta) = \begin{bmatrix} \cos(\theta) & -\sin(\theta) \\ \sin(\theta) & \cos(\theta) \end{bmatrix}$
Linear Polarizer (LP)	$J_{pol}(p_x, p_y) = \begin{bmatrix} p_x & 0 \\ 0 & p_y \end{bmatrix}$, $0 \leq p_x, p_y \leq 1$
LP: Transmission along x-axis	$J_{pol}(1,0) = \begin{bmatrix} 1 & 0 \\ 0 & 0 \end{bmatrix}$
LP: Transmission along y-axis	$J_{pol}(0,1) = \begin{bmatrix} 0 & 0 \\ 0 & 1 \end{bmatrix}$
LP: Transmission axis at angle θ with x-axis	$\mathcal{R}(\theta) J_{pol}(1,0) \mathcal{R}(-\theta)$
Phase Retarder (Fast Axis: Horizontal)	$J_{pr}(\Delta\phi) = \begin{bmatrix} e^{-i\frac{\Delta\phi}{2}} & 0 \\ 0 & e^{i\frac{\Delta\phi}{2}} \end{bmatrix}$
Half Wave Plate (Fast Axis: Horizontal)	$J_{pr}(\pi) = \begin{bmatrix} -i & 0 \\ 0 & i \end{bmatrix}$
Quarter Wave Plate (Fast Axis: Horizontal)	$J_{pr}\left(\frac{\pi}{2}\right) = \begin{bmatrix} e^{-i\frac{\pi}{4}} & 0 \\ 0 & e^{i\frac{\pi}{4}} \end{bmatrix}$
Phase Retarder (Fast Axis: angle θ with x-axis)	$\mathcal{R}(\theta) J_{pr}(\Delta\phi) \mathcal{R}(-\theta)$

Table A.2: Jones Matrices of Optical Elements

Optical Process	**Jones Matrix**
Mirror reflection	$J_M(R, \delta) = \sqrt{R} \begin{bmatrix} -e^{i\delta/2} & 0 \\ 0 & e^{-i\delta/2} \end{bmatrix}$
Transmission through chiral substance	$\begin{bmatrix} \cos(\theta_{cr}) & -\sin(\theta_{cr}) \\ \sin(\theta_{cr}) & \cos(\theta_{cr}) \end{bmatrix}$
Linear Birefringence with birefringence axis at θ_{br}	$\mathcal{R}(\theta_{br}) J_{pr}(\Delta\phi_{br}) \mathcal{R}(-\theta_{br})$

Table A.3: Jones matrices of Optical processes

A.3 Linear Birefringence

In general, materials have non-uniform structure. As a result, there are axes developed inside the material with different refractive indices for the two orthogonal linear polarizations (often called s from the german *senkrecht* and p from *parallel*). Since light can be expressed as a superposition of s and p polarization eigenvectors, when polarized light emerges through a linear birefringent material its components experience different refraction coefficient leading to phase retardation. Phase retardation between the s and p components changes the state of polarization of light.

At molecules or crystals there often exist an axis of symmetry that defines a direction where both $\vec{\mathbf{E}}$-vibrations interact with the electrons in the same way when traveling through it. This direction of symmetry through the crystal is called the optic axis (OA) of the crystal. The $\vec{\mathbf{E}}$-components of light traveling through OA "see" no anisotropy and as a result, there is no phase difference between them.

A birefringent crystal can be cut and polished to produce polarizing elements in which the OA may have any desired orientation relative to the incident light [28].

When light propagates through the OA both beams propagate with the same speed with an index of refraction n. When OA is at a random angle with the direction of propagation each component propagates through the crystal with a different index of refraction and speed. If the thickness of the crystal is d the difference in optical paths is

$$\Delta = |n_s - n_p|d \tag{A.8}$$

and the corresponding phase difference is

$$\Delta\phi = 2\pi \left(\frac{\Delta}{\lambda_0}\right) \tag{A.9}$$

where λ_0 is the vacuum wavelength. In the case of a quarter-wave plate $\Delta\phi = \pi/2$ and in the case of a half-wave plate $\Delta\phi = \pi$.

Appendix B

Non-planarity Induced Optical Rotation

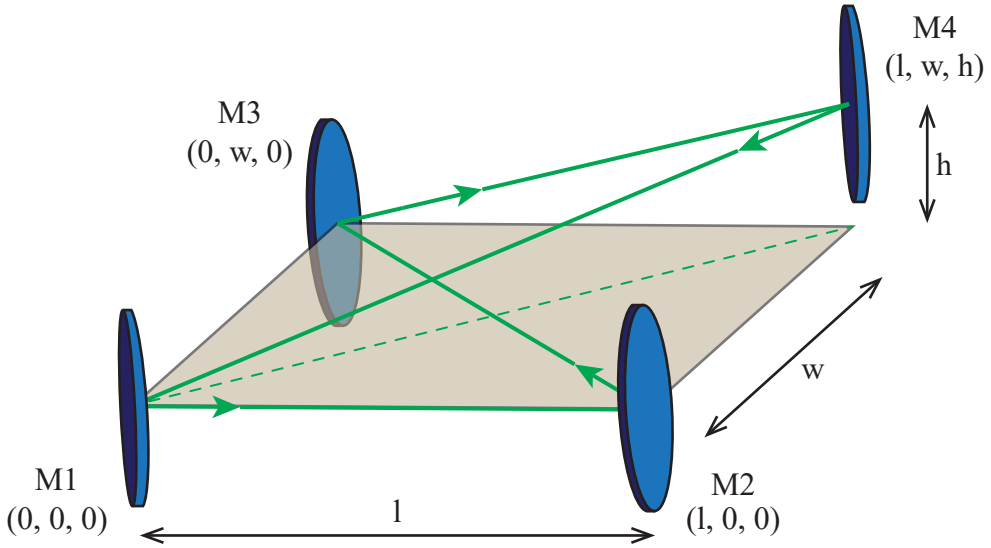

Figure B.1: The coordinate system and geometry light path used for describing propagation of light inside the bowtie cavity. Non-planar chiral rotation is induced by bringing mirror M4 out of the plane defined by the remaining three mirrors.

A non-planar cavity configuration (i.e. a four-mirror cavity configuration in which one of the mirrors is out of plane defined by the other three) introduces a chiral rotation to the polarization of the radiation traveling inside the cavity. The non-planarity induced optical rotation (NPI-OR) has been utilized in the construction of monolithic non-planar ring oscillators, as well as in high finesse cavities used for the production of high-intensity gamma-ray fluxes by pulsed laser beam Compton scattering [29, 30]. However, **unintentional** NPI-OR, mainly due to misalignment of the CW and CCW beams relative to the optical axis of the cavity, is also a potential source of a systematic offset to the optical rotation measurement in CRDP technique. In the following, we present the results of a theoretical model produced by Bougas et.al. [25].

For a bowtie cavity with the geometry shown in Figure B.1, and under the assumptions $l > w \gg h$, we obtain a closed analytical expression for the NPI-OR angle, for the CW

propagation direction,

$$\alpha_c = \sin^{-1}\left(\frac{\left(-l+\sqrt{l^2+w^2}\right)\gamma}{w}\right) \tag{B.1}$$

where $\gamma = \tan^{-1}(h/l)$, h is the off-plane height of M4, w is the distance between M2 and M4 (M1 and M3) and l is the distance between M1 and M2 (M3 and M4). For $w \gg l$, we get

$$\alpha_c = \sin^{-1}\left(\frac{wh}{l^2}\right) \tag{B.2}$$

The chiral nature of the NPI-OR is verified since reversing the ordering (CCW propagation) the sign of polarization rotation is reversed.

Appendix C

Gaussian Beams

Although the light emitted by the laser is usually designed as a ray, this does not constitute a complete and spherical interpretation of its wave nature. It is necessary to obtain a wave description of light where quantities like amplitude, phase, and spatial extent are explicitly declared.

In this chapter, a brief presentation of Gaussian beams is given. At first, a mathematical derivation using Maxwell equations will be given. Next, we will discuss the most important and frequently occurred in experimental applications mode, TEM_{00}. This chapter is based on the book by J.T. Verdeyen, *Laser Electronics* [14].

C.1 Mathematical Derivation of TEM modes

Most optical beams propagating in free space are almost pure TEM (transverse electric and magnetic), meaning that the spatial field component lies perpendicular to the direction of propagation. This can be easily shown by the Maxwell equations for free space:

$$\nabla \cdot \mathbf{E} = 0 \tag{C.1a}$$

$$\nabla \cdot \mathbf{B} = 0 \tag{C.1b}$$

In the following derivation we will use only the electric field $\mathbf{E}$ as both fields are connected through Maxwell equations.

The wave equation of the electric field is:

$$\nabla^2 \mathbf{E} = \frac{1}{v^2} \frac{\partial^2 \mathbf{E}}{\partial t^2} \tag{C.2}$$

where $v = c/n$ is the velocity inside a medium with index of refraction n.

The time-independent component of (C.2), known as Helmholtz equation, is:

$$\nabla^2 E + \frac{\omega^2}{c^2} n^2 E = 0 \tag{C.3}$$

Equation (C.3) can be written as:

$$\nabla_t^2 E + \frac{\partial^2 \mathbf{E}}{\partial z^2} + \frac{\omega^2}{c^2} n^2 E = 0 \tag{C.4}$$

where we used the fact that the divergence operation can be broken up into transverse divergence (∇_t) of the transverse field E_t and the longitudinal derivation of the z component of the field.

We will seek for solutions of the form:

$$E = E_0 \psi(x, y, z) e^{-ikz} \tag{C.5}$$

where $k = \omega n/c$. The factor E_0 is the amplitude, closely related with the light intensity, the exponential factor expresses our feelings that the wave should be approximated with a uniform plane wave and the function ψ measures how the beam deviates from a uniform plane wave.

Substituting (C.5) in (C.4) we obtain:

$$\nabla_t^2 \psi - i2k \frac{\partial \psi}{\partial z} + \frac{\partial^2 \psi}{\partial z^2} = 0 \tag{C.6}$$

Since k is a very large number in optical frequencies, the term with the second derivative can be neglected as it is multiplied with the unity, whereas the term with the first derivative is multiplied by k. As a result we obtain the central equation for Gaussian beams, called paraxial equation:

$$\nabla_t^2 \psi - i2k \frac{\partial \psi}{\partial z} = 0 \tag{C.7}$$

C.2 Mode TEM$_{00}$

What differentiates TEM$_{00}$ mode from higher order modes is the fact that TEM$_{00}$ is assumed to by cylindrically symmetric. As a result, equation (C.7) can be written as:

$$\frac{1}{r} \frac{\partial}{\partial r} \left(r \frac{\partial \psi}{\partial r} \right) - i2k \frac{\partial \psi}{\partial z} = 0 \tag{C.8}$$

The "ansatz" we choose for (C.8) is:

$$\psi(r, z) = \exp \left[-i \left(P(z) + \frac{kr^2}{2q(z)} \right) \right] \tag{C.9}$$

where $P(z)$ and $q(z)$ are functions need to be determined.

Substituting (C.9) in (C.8) we obtain for the spatial component of the electric field for the TEM$_{00}$ mode:

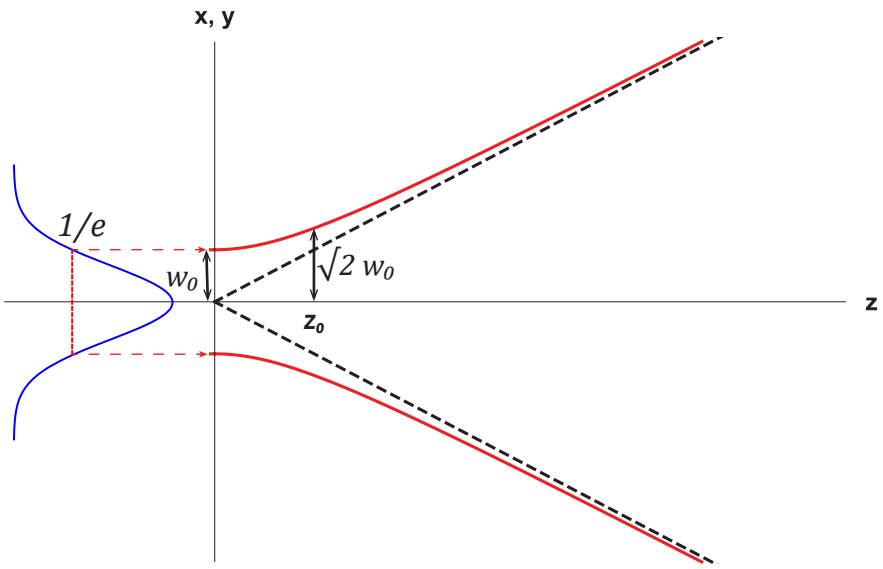

Figure C.1: Spreading of a TEM_{00} along the direction of propagation. The distance z_0 is the "Rayleigh length". At $z = z_0$ the spot size $w(z_0) = \sqrt{2}w_0$. Twice the value of Rayleigh length is consider the beam length before it rapidly expands.

$$E(x,y,z) = \underbrace{E_0\left(\frac{w_0}{w(z)}e^{-r^2/w^2(z)}\right)}_{\text{amplitude factor}} \times \underbrace{\exp\left[-i\left(kz - \tan^{-1}\left(\frac{z}{z_0}\right)\right)\right]}_{\text{longitudinal phase}} \times \underbrace{\exp\left[-i\frac{kr^2}{2R(z)}\right]}_{\text{radial phase}} \tag{C.10}$$

where

$$w^2(z) = w_0^2\left[1 + \left(\frac{\lambda_0 z}{\pi n w_0^2}\right)^2\right] = w_0^2\left[1 + \left(\frac{z}{z_0}\right)^2\right] \tag{C.11}$$

$$R(z) = z\left[1 + \left(\frac{\pi n w_0^2}{\lambda_0 z}\right)^2\right] = z\left[1 + \left(\frac{z_0}{z}\right)^2\right] \tag{C.12}$$

$$z_0 = \frac{\pi n w_0^2}{\lambda_0} \tag{C.13}$$

Also:

$$\frac{1}{q(z)} = \frac{1}{R(z)} - i\frac{\lambda_0}{\pi n w^2(z)} \tag{C.14}$$

We note that the distance z_0 is often called "Rayleigh length". At $z = z_0$ the spot size $w(z_0) = \sqrt{2}w_0$. Twice the value of Rayleigh length is consider the beam length before it rapidly expands.

The first term in (C.10) describes the dependence of the amplitude of the field from the

the radial coordinate and shows how the beam propagates along the propagation axis, z. We note that at $r = w$ the field is reduced by $1/e$ of its preak value E_0 at $(x, y, z) = (0, 0, 0)$. In Figure C.1 the spot size $w(z)$ is depicted. We observe that as z becomes larger, the e^{-1} points become farther from the axis. Specifically for large z ($z \gg z_0$) the spot size of the beam is asymptotic to the dashed lines described by:

$$w(z \gg z_0) = \frac{w_0 z}{z_0} = \frac{\lambda_0 z}{\pi n w_0} \tag{C.15}$$

The second factor of (C.10) expresses the change in the phase of the wave in the direction of propagation

$$\phi = kz - \tan^{-1}\left(\frac{z}{z_0}\right) \tag{C.16}$$

which differs from that of a uniform plane wave by the factor $\tan^{-1}(z/z_0)$.

The third factor of (C.10) shows that the plane $z =$ constant does not represent an equiphase surface, as is the case for plane waves. In contrast, the equiphase surfaces are spherical with a radius of curvature given by $R(z)$. It is worth noting the in Gaussian beams, the center for the curved wave-front changes as well as at $z = 0$ the curvature $R(z = 0) \to \infty$ (plane wavefront).

For the sake of completeness, we present the relationship for higher order modes, $\mathrm{TEM}_{m,p}$:

$$\begin{aligned} E(x, y, z) = E_{m,p} H_m \left[\frac{2^{1/2} x}{w(z)}\right] H_p \left[\frac{2^{1/2} y}{w(z)}\right] \\ \times \frac{w_0}{w(z)} \exp\left[-\frac{x^2 + y^2}{w^2(z)}\right] \\ \times \exp\left[-i\left(kz - (1 + m + p)\tan^{-1}\left(\frac{z}{z_0}\right)\right)\right] \\ \times \exp\left[-i\frac{kr^2}{2R(z)}\right] \end{aligned} \tag{C.17}$$

where $H_m(\xi)$ stands for the Hermite polynomial of order m:

$$H_m(\xi) = (-1)^m e^{\xi^2} \frac{d^m e^{-\xi^2}}{d\xi^m} \tag{C.18}$$

C.3 Gaussian Beams in Optical Cavities

As it is explained in Chapter 3, stable optical cavities are configurations consisting of mirrors which trap light between them. This is possible only when the spatial characteristics of the light beam are in agreement with conditions determined by the geometrical characteristics of the cavity. When the light inserting the cavity has a Gaussian spatial profile then stability occurs when the surfaces of the mirrors exactly match the surfaces of constant phase of the beam. For this purpose, it is a common practice to place lenses before the cavity entrance in order to modify the spatial characteristics of the Gaussian

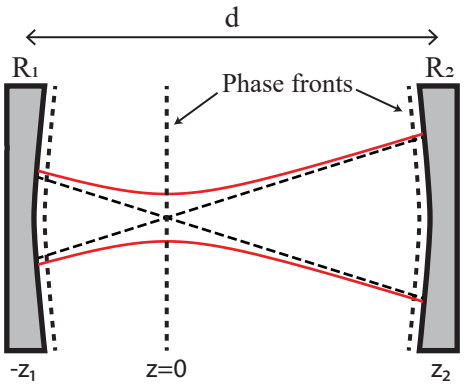

Figure C.2: Simple stable, two-mirror cavity of length $d = z_1 + z_2$. The radius of curvature of the beam going to the right matches the surface of R_2 and simultaneously to the left it matches R_1.

beam.

For instance, in a two-mirror cavity (Figure C.2) of length d, with mirror curvatures R_1, R_2 at positions z_1, z_2 respectively, the Gaussian beam should be such that the radius of curvature of the beam going to the right matches the surface of R_2 and simultaneously to the left matches R_1. Since the rays associated with this Gaussian beam impinge perpendicular to the mirror surface, they will be reflected back on themselves and return to the other, leading to a normal mode of this cavity.

As a result we have a system of three equations:

$$z_1 + z_2 = d \tag{C.19}$$

$$R(z_1) = -R_1 = -z_1 \left[1 + \left(\frac{z_0}{z_1}\right)^2\right] \tag{C.20}$$

$$R(z_2) = R_2 = z_2 \left[1 + \left(\frac{z_0}{z_2}\right)^2\right] \tag{C.21}$$

We note that in equation (C.20) we placed the minus sign in front of R_1 since we know that the left mirror has a positive radius of curvature (focusing) but the wavefront has a mathematical negative radius of curvature since it is on the left of $z = 0$.

Solving the above system we obtain the following equations for z_0, z_1, z_2:

$$z_0^2 = \left(\frac{\pi w_0^2}{\lambda_0}\right)^2 = \frac{d(R_1 - d)(R_2 - d)(R_1 + R_2 - d)}{(R_1 + R_2 - 2d)^2} \tag{C.22}$$

$$z_1 = \frac{d(R_2 - d)}{R_1 + R_2 - 2d} \tag{C.23}$$

$$z_2 = \frac{d(R_1 - d)}{R_1 + R_2 - 2d} \tag{C.24}$$

Forcing the phase fronts to coincide with the mirror surface is successful for stable cavities but becomes complicated for complex systems. For that reason, there is another way to handle optical cavities using the ABCD law, presented thoroughly in [14].

Bibliography

[1] Dimitris Sofikitis, Lykourgos Bougas, Georgios E. Katsoprinakis, Alexandros K. Spiliotis, Benoit Loppinet, and T. Peter Rakitzis. Evanescent-wave and ambient chiral sensing by signal-reversing cavity ringdown polarimetry. *Nature*, 514(7520):76–79, September 2014.

[2] Lord Kelvin (W.H. Thomson). Baltimore lectures on molecular dynamics and the wave theory of light. *C.J. Clay and Sons, Cambridge University Press Warehouse*, page 619, 1904.

[3] Albert Guijarro and Miguel Yus. *The Origin of Chirality in the Molecules of Life*. The Royal Society of Chemistry, 2009.

[4] L.D. Barron. True and false chirality and parity violation. *Chemical Physics Letters*, 123(5):423–427, 1986.

[5] Francois Arago. *"Mémoire sur une modification remarquable qu'éprouvent les rayons lumineux dans leur passage à travers certains corps diaphanes et sur quelques autres nouveaux phénomènes d'optique"*, volume 1. Mémoires de la classe des sciences mathématiques et physiques de l'Institut Impérial de France, 1811.

[6] N.B. Baranova and B.Ya. Zel'Dovich. Theory of a new linear magnetorefractive effect in liquids. *Molecular Physics*, 38(4):1085–1098, 1979.

[7] G. Wagnière and A. Meier. Difference in the absorption coefficient of enantiomers for arbitrarily polarized light in a magnetic field: A possible source of chirality in molecular evolution. *Experientia*, 39(10):1090–1091, October 1983.

[8] G. L. J. A. Rikken and E. Raupach. Observation of magneto-chiral dichroism. *Nature*, 390(6659):493–494, December 1997.

[9] G. L. J. A. Rikken and E. Raupach. Enantioselective magnetochiral photochemistry. *Nature*, 405(6789):932–935, June 2000.

[10] Marie-Anne Bouchiat and Claude Bouchiat. Parity violation in atoms. *Reports on Progress in Physics*, 60(11):1351–1396, November 1997.

[11] Dimitris Sofikitis, George E. Katsoprinakis, Alexandros K. Spiliotis, and T. Peter Rakitzis. Chapter 16: Cavity-based chiral polarimetry. In Prasad L. Polavarapu, editor, *Chiral Analysis*, pages 649–678. Elsevier, second edition, 2018.

[12] D. Y. Smith. Comments on the dispersion relations for the complex refractive index of circularly and elliptically polarized light. *J. Opt. Soc. Am.*, 66(5):454–460, May 1976.

[13] P. Molina, V. Vasyliev, E. G. Víllora, and K. Shimamura. Cef3 and prf3 as uv-visible faraday rotators. *Opt. Express*, 19(12):11786–11791, Jun 2011.

[14] J.T. Verdeyen. *Laser Electronics*. Prentice Hall, 1995.

[15] Anna Karaiskou, Vassilis Papadakis, Benoit Loppinet, and T. Peter Rakitzis. Cavity ring-down ellipsometry. *The Journal of Chemical Physics*, 131(12):121101, 2009.

[16] Michael A. Everest, Vassilis M. Papadakis, Katerina Stamataki, Stelios Tzortzakis, Benoit Loppinet, and T. Peter Rakitzis. Evanescent-wave cavity ring-down ellipsometry. *The Journal of Physical Chemistry Letters*, 2(11):1324–1327, May 2011.

[17] Katerina Stamataki, Vassilis Papadakis, Michael A. Everest, Stelios Tzortzakis, Benoit Loppinet, and T. Peter Rakitzis. Monitoring adsorption and sedimentation using evanescent-wave cavity ringdown ellipsometry. *Appl. Opt.*, 52(5):1086–1093, Feb 2013.

[18] Dimitrios Sofikitis, Katerina Stamataki, Michael Everest, Vassilis Papadakis, Jean-Louis Stehlé, Benoit Loppinet, and T. Rakitzis. Sensitivity enhancement for evanescent-wave sensing using cavity-ring-down ellipsometry. *Optics Letters*, 38:1224–1226, 04 2013.

[19] D. Sofikitis, A. K. Spiliotis, K. Stamataki, G. E. Katsoprinakis, L. Bougas, P. C. Samartzis, B. Loppinet, T. P. Rakitzis, M. Surligas, and S. Papadakis. Microsecond-resolved sdr-based cavity ring down ellipsometry. *Appl. Opt.*, 54(18):5861–5865, Jun 2015.

[20] Wolfgang Demtröder. *Laser Spectroscopy*. Springer Berlin Heidelberg, 2003.

[21] Thomas Müller, Kenneth B. Wiberg, and Patrick H. Vaccaro. Cavity ring-down polarimetry (CRDP): a new scheme for probing circular birefringence and circular dichroism in the gas phase. *The Journal of Physical Chemistry A*, 104(25):5959–5968, June 2000.

[22] Thomas Müller, Kenneth B. Wiberg, Patrick H. Vaccaro, James R. Cheeseman, and Michael J. Frisch. Cavity ring-down polarimetry (crdp): theoretical and experimental characterization. *J. Opt. Soc. Am. B*, 19(1):125–141, Jan 2002.

[23] Jérôme Poirson, Marc Vallet, Fabien Bretenaker, Albert Le Floch, and Jean-Yves Thépot. Resonant cavity gas-phase polarimeter. *Analytical Chemistry*, 70(21):4636–4639, October 1998.

[24] A.K. Spiliotis, M. Xygkis, E. Klironomou, E. Kardamaki, G.K. Boulogiannis, G.E. Katsoprinakis, D. Sofikitis, and T.P. Rakitzis. Optical activity of lysozyme in solution at 532 nm via signal-reversing cavity ring-down polarimetry. *Chemical Physics Letters*, 747:137345, 2020.

[25] Lykourgos Bougas, Dimitris Sofikitis, Georgios E. Katsoprinakis, Alexandros K. Spiliotis, Paraskevas Tzallas, Benoit Loppinet, and T. Peter Rakitzis. Chiral cavity ring down polarimetry: Chirality and magnetometry measurements using signal reversals. *The Journal of Chemical Physics*, 143(10):104202, September 2015.

[26] A K Spiliotis, M Xygkis, E Klironomou, E Kardamaki, G K Boulogiannis, G E Katsoprinakis, D Sofikitis, and T P Rakitzis. Gas-phase optical activity measurements using a compact cavity ringdown polarimeter. *Laser Physics*, 30(7):075602, jun 2020.

[27] R. Clark Jones. A new calculus for the treatment of optical systems. *J. Opt. Soc. Am.*, 31(7):488–493, Jul 1941.

[28] Frank L Pedrotti, Leno S Pedrotti, and Leno M Pedrotti. *Introduction to Optics*. Pearson, Upper Saddle River, NJ, 3 edition, April 2006.

[29] A.C. Nilsson, E.K. Gustafson, and R.L. Byer. Eigenpolarization theory of monolithic nonplanar ring oscillators. *IEEE Journal of Quantum Electronics*, 25(4):767–790, 1989.

[30] J Bonis, R Chiche, R Cizeron, M Cohen, E Cormier, P Cornebise, N Delerue, R Flaminio, D Jehanno, F Labaye, M Lacroix, R Marie, B Mercier, C Michel, Y Peinaud, L Pinard, C Prevost, V Soskov, A Variola, and F Zomer. Non-planar four-mirror optical cavity for high intensity gamma ray flux production by pulsed laser beam compton scattering off GeV-electrons. *Journal of Instrumentation*, 7(01):P01017–P01017, January 2012.